TAMPEREEN TEKNILLINEN YLIOPISTO
TAMPERE UNIVERSITY OF TECHNOLOGY

SILVIA RUBIO PEREGRINA

CAVITATION AND SLURRY EROSION WEAR OF THERMALLY SPRAYED HARDMETAL COATINGS

Master of Science thesis

Examiners: prof. Petri Vuoristo, MSc (Tech) Ville Matikainen
Examiners and topic approved by the Faculty Council of the Faculty of Engineering Sciences
on 26th April 2017

ABSTRACT

SILVIA RUBIO PEREGRINA: Cavitation and Slurry Erosion Wear of Thermally Sprayed Hardmetal Coatings
Tampere University of Technology
Master's Thesis, 76 pages
September 2017
Master's Degree Erasmus Exchange Student
Major: Materials Engineering
Examiners: prof. Petri Vuoristo, MSc (Tech) Ville Matikainen

Keywords: Thermal spray, hardmetal, coating, cavitation erosion, slurry erosion

Thermally sprayed coatings are used to protect and provide life extension to components intended to perform in aggressive conditions such as extreme temperatures, wear and corrosive environments. In the present study two hardmetal compositions, Cr_3C_2-25NiCr and WC-10Co4Cr, were thermally sprayed with three different technologies: high-velocity oxygen fuel (HVOF) with gas or liquid fuel and high-velocity air fuel (HVAF) spray process. The samples were exposed to slurry and cavitation erosion conditions using a pin mill slurry pot unit and a vibratory apparatus, respectively. The slurry pot tests were performed with two different abrasive particle sizes. Besides the volume loss results obtained, SEM micrographs of the surface coatings were taken before and after the tests to study the erosion mechanisms. Regarding cavitation erosion, HVAF coatings were the best performing ones, followed by liquid fuel HVOF coatings. The same trend was observed for slurry erosion test results but with some exceptions, e.g. one of the HVAF coatings of Cr_3C_2-25NiCr presented bigger volume loss than the HVOF coatings. In addition, the liquid fuel HVOF sprayed coatings of WC-10Co4Cr were the worst performing in the test with coarse erodent particles.

PREFACE

This Master's thesis was prepared during my Erasmus exchange at Tampere University of Technology. I would like to express my appreciation to MSc (Tech) Ville Matikainen for his valuable guidance and advices throughout the project. I would also like to thank Professor Petri Vuoristo for considering me for this research work and for carrying out the examination.

Madrid, 22.8.2017

Silvia Rubio Peregrina

CONTENTS

LIST OF ABBREVIATIONS

BSE	Back Scattered Electron image
Cr_3C_2	Chromium carbide
HVAF	High-velocity air fuel
HVOF	High-velocity oxyfuel
SEM	Scanning Electron Microscope
WC	Tungsten carbide

LIST OF FIGURES

LIST OF TABLES

1. PURPOSE AND OBJECTIVE

The purpose of this thesis is to compare two types of hardmetal compositions sprayed by three different thermal spray technologies in terms of cavitation and slurry erosion resistance. The compositions used for the hardmetal coatings are Cr_3C_2-25NiCr and WC-10Co4Cr and the thermal spray technologies are gas fuel high-velocity oxyfuel (gas fuel HVOF), liquid fuel high-velocity oxyfuel (liquid fuel HVOF) and high-velocity air fuel (HVAF). HVAF process is the latest development stage of combustion based high velocity spray processes and has shown good performance in different erosive tests [1]-[3]. It could be a better alternative to the HVOF techniques. Therefore, this research aims to study the properties and performance of the HVAF coatings against cavitation and slurry erosion.

In order to do so, the objective is to carry out cavitation erosion tests and slurry erosion tests on the thermally sprayed coatings. After performing the tests, information of volume loss is obtained and SEM images of the eroded surfaces are taken. Micrographs will be analysed to describe the wear mechanisms involved and together with the volume loss data, it will be determined which technology produces the best performing coatings.

2. THEORETICAL BACKGROUND

This section serves as an introduction of the studied topic that gives the necessary background to follow the thesis. First, hardmetals are described, then thermal spray is defined taking into account the available technologies, having HVOF and HVAF their own subsections for further insight. Finally, the phenomena of cavitation and slurry erosion are addressed, as well as the different test apparatus found in the literature.

2.1 Hardmetals

Hardmetals or cemented carbides are composite materials made of a ceramic hard phase embedded in a metallic soft phase. They are a range of very hard, refractory and wear-resistant alloys whose development started in the early years of the 20th century. By this time it was discovered that the presence of hard carbide particles, namely tungsten carbide, in the metallic matrix of high-speed steel resulted in outstanding machining capabilities. After the First World War, new materials were investigated for the dies used to draw tungsten filament wire for light bulbs at the Osram works in Germany. After several attempts, Schröter found out that if tungsten carbide powder was mixed with metals such as iron, nickel or cobalt, the sintered product presented low porosity, high hardness and considerable strength. The findings were gathered in the Schröter patent in 1923 [4]-[6].

Regarding thermally sprayed hardmetal coatings, the first deposition was reported by Schoop in 1942 using an arc spray process. Nowadays, HVOF is the industrial standard technology for preparation of hardmetal coatings, which are used for wear protection in different fields of industry. The resulting coatings present a typical thickness within the range of 100-500 μm and they are prepared from feedstock powders with a particle size range of 10-45 μm, as shown in Figure 1 [7].

The main available compositions are WC–12Co, WC–17Co, WC–10Co–4Cr, WC–20“CrC”–7Ni and Cr_3C_2–(20–25)NiCr, in which tungsten carbide (WC) and chromium carbide (Cr_3C_2) act as the hard phase. Tungsten carbide is used in components that undergo abrasive wear such as hydroturbine blades or pipelines, while nickel-bonded chromium carbide serves as protection to devices exposed to both corrosion and abrasion in the chemical and process industries. However, chromium carbide abrasion resistance is lower than that of tungsten carbide [4], [7].

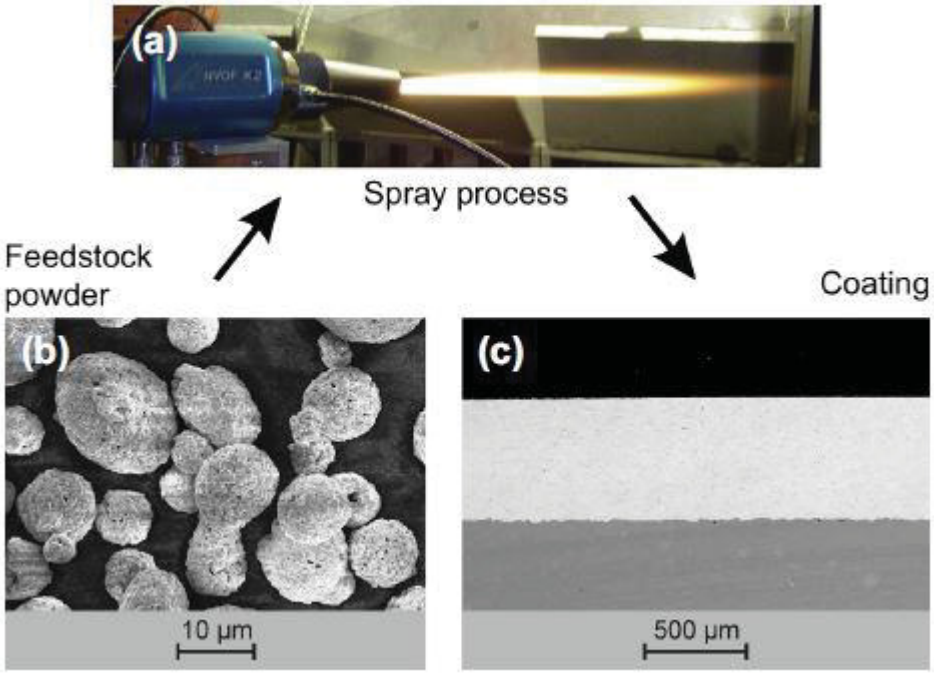

Figure 1. *Illustration of hardmetal coating preparation by the HVOF spray process. (a) HVOF spray gun, (b) SEM of agglomerated and sintered feedstock powder WC-17Co, (c) Dense WC-Co coating [7].*

Several studies prove the satisfactory wear strength of hardmetal coatings, but these also differ in the optimum hard phase/matrix ratio to achieve the maximum erosion resistance. Kulu and Pihl [8] observed that at low and medium impact angles the carbide phase must be greater than 50% and in the case of an impact angle near to 90º, hard phase should be less than 50% to experiment the lowest wear rates. Levy [9] stated that a minimum of 80% of hard phase is necessary to provide maximum erosion protection. In support of Levy, Walsh and Tabakoff [10] have shown that a coating made from a powder containing 80 wt.% chromium carbide is more erosion resistant than one with 65 wt.% chromium carbide. Besides, Lewis et al. [11] reported an increase in the erosion resistance of hardmetal coatings when increasing the amount of chromium carbide in the pre-sprayed powder. However, contrary results are found in studies dealing with tungsten carbide. For instance, Tu et al. [12] concluded the optimum amount of 35% of tungsten carbide in the pre-sprayed powder for erosion resistance. Moreover, Wang et al. [13] observed an increase of the erosion rate when the percentage of tungsten carbide in the coating increased from 7% to 16%.

After introducing hardmetal coatings, thermal spray technology is described in the following subsection.

2.2 Thermal spraying

Thermal spraying is a process in which molten, semi-molten or even solid particles are deposited on a substrate to form a coating. These particles are propelled in a gas stream

that provides them with thermal and kinetic energy, allowing them to plastically deform when impacting on the substrate or underlying coating. As illustrated in Figure 2, in order to obtain the coating, a feedstock material usually in the form of powder, stick or wire is melted by the heat source and particles are accelerated towards the substrate deforming and flattening during the impact. The coatings obtained are used to protect and provide life extension to components intended to perform in aggressive conditions such as extreme temperatures, wear and corrosive environments [14]-[16].

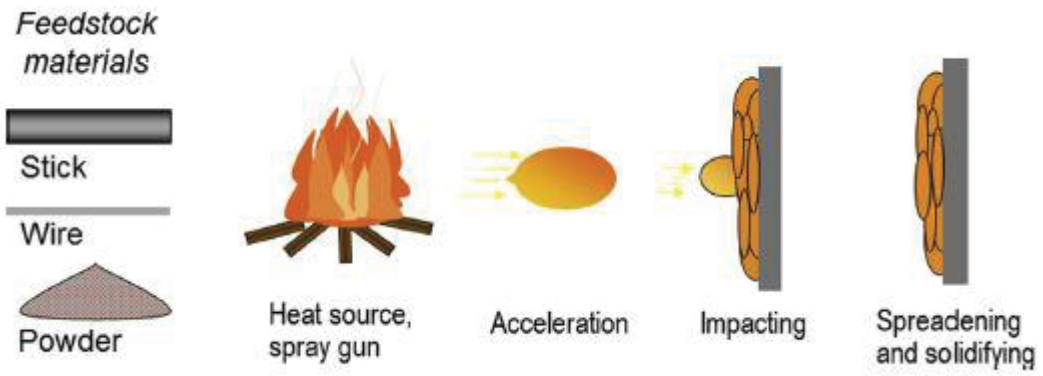

Figure 2. *Principle of thermal spraying [14].*

Thermal spraying includes several types of processes that can be classified according to the energy source used to melt the feedstock material. Technologies such as flame spraying, detonation-gun spraying and high velocity flame spraying are based on the combustion of gases. Electric discharge energy is used as heat source in electric arc spraying and plasma spraying and the cold kinetic spraying technique is based on the decompression of gases [14].

Flame spraying was the first thermal spraying developed in the beginning of the 20th century by the Swiss engineer Dr. M. U. Schoop and his associates. As it has already been mentioned, this technology uses the chemical energy of combusting fuel gases to melt the feedstock material. The most common torches are those using acetylene as the main fuel with oxygen to achieve the highest combustion temperatures. Wires are introduced axially to the torch and powders can be fed axially or perpendicularly through the rear of the nozzle. The materials used to be deposited range from polymers to ceramics and refractory metals. A schematic of a powder flame spraying torch is shown in Figure 3 [14], [15], [17].

The detonation-gun spraying process (D-gun) was developed by Union Carbide (now Praxair Surface Technologies) in the early 1950s and in the 1960s at the Paton Institute in Kiev (Ukraine). In detonation-gun spray equipment, a mixture of acetylene, oxygen and a charge of powder is fed into a long water cooled barrel, as shown schematically in Figure 4. A spark plug ignites the gas producing a detonation wave that accelerates the powder to supersonic velocity achieving denser coatings than was possible with the flame spraying process. Nitrogen or air is used to purge the barrel after each detonation. In this process, the most used powders are composites with carbide reinforcement [14], [15], [17].

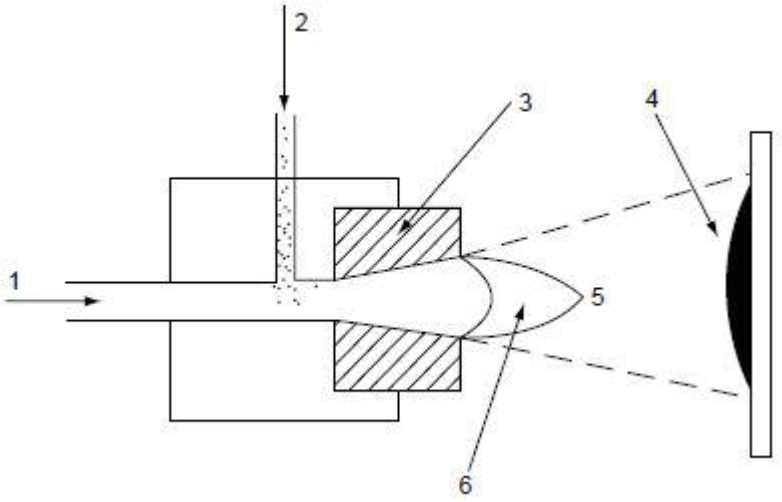

Figure 3. *Schematic of a powder flame spraying torch: (1) working gases (fuel and oxygen); (2) injection of powder; (3) torch body; (4) sprayed coating; (5) stream of particles; (6) combustion flame [15].*

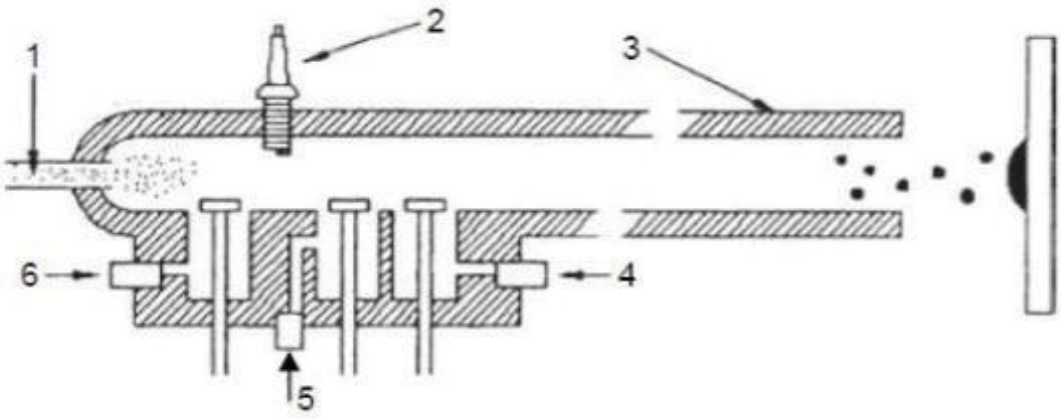

Figure 4. *Schematic of a detonation-gun spray equipment: (1) powder injection; (2) spark plug; (3) gun barrel; (4) oxygen input; (5) nitrogen input [15].*

High velocity flame spraying includes different kinds of processes that use an expansion nozzle after the combustion chamber leading to high kinetic energies. High particle velocities allow working with moderate temperatures, since thermal energy is partly replaced by kinetic energy. These temperatures are lower than in many other spray processes, which results in a low amount of oxidation in the case of metallic and hardmetal coatings. The high deposition velocities lead to a dense and well-adhered coating. The most common technologies are high-velocity oxygen fuel spraying (HVOF) using gas or liquid fuel and high-velocity air fuel (HVAF). These techniques will be described in detail in the following sections 2.3 and 2.4 [14].

Electric arc spraying was developed by Dr. M. U. Schoop approximately in 1910 but it was not until the early 1960s when it gained commercial acceptance. In this method, an electric arc is formed between the gap of two consumable electrode wires that are melted and then atomised and propelled by a compressed gas, usually air, towards the substrate. Due to its working principle, feedstock material must be electrically conductive like metals, metal alloys, metal-metal oxide or metal-carbide mixtures. Figure 5 shows the schematic of an arc spraying gun [14], [15], [17].

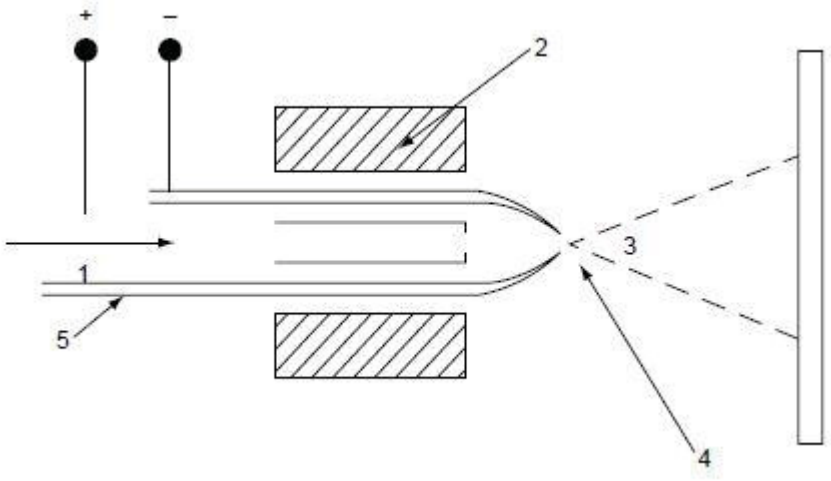

Figure 5. *Schematic of an arc spraying installation: (1) atomising gas flow; (2) torch outer shield; (3) stream of molten particles; (4) electric arc; (5) consumable arc electrodes [15].*

Plasma spraying was patented in 1960 by Giannini and Ducati [18], as well as by Gage et al. in 1962 [19]. Plasma, which usually consists of neutral atoms, positive ions and free electrons, can be achieved when transferring enough energy to a gas to ionize it allowing ions and electrons to act independently from one another. In this state, plasma is obtained by applying an electric field that will sustain currents as the free electrons move through the ionized gas. If at this point, the input energy is removed, electrons and ions will recombine releasing heat and light energy [15], [17].

Plasma spraying uses an electric discharge to ionize the working gases which after recombining transform into high energy gas jets to produce dense coatings. This technology is the most flexible regarding the materials that can be sprayed due to its high temperature heat source, making possible to melt practically all kinds of materials like ceramics and refractory metals. Argon and nitrogen are used as primary process gases, as they ionize easily, and hydrogen and helium as secondary process gases to increase the enthalpy enabling an efficient melting capacity of the plasma torch. There are several types of plasma processes, atmospheric plasma spraying and vacuum plasma spraying being the most common ones. Figure 6 shows a schematic of an atmospheric plasma torch [14].

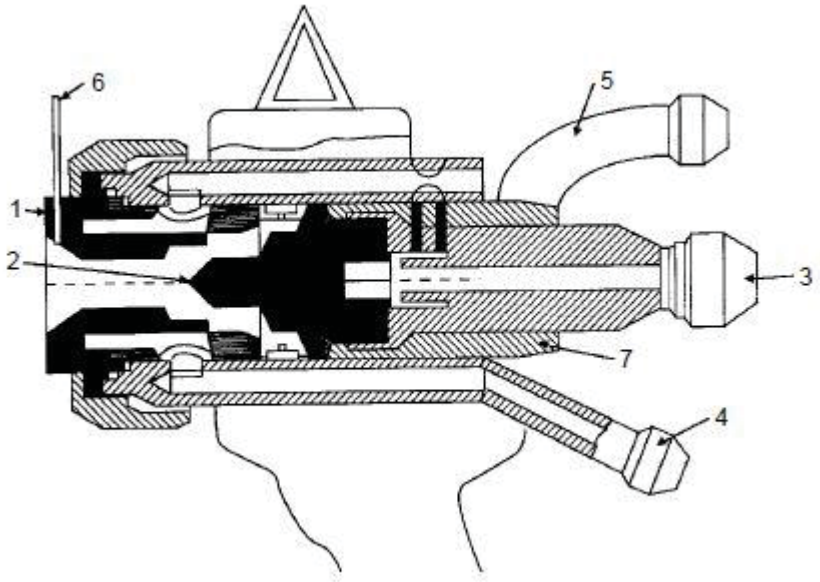

Figure 6. *Schematic of an atmospheric plasma torch: (1) anode; (2) cathode; (3) water outlet and cathode connector; (4) water inlet and anode connector; (5) inlet for working gases; (6) powder injector; (7) electrical insulator [15].*

The decompression of gases is used as heat source in the cold kinetic spraying or cold gas spraying, a method developed in Russia at the end of the 1980s by Alkhimov *et al.* [20]. This process differs from the rest of the thermal spray techniques because the working temperatures are below the melting point of the feedstock material, i.e. the sprayed particles remain in a solid state. The particles deform when impacting on the substrate thanks to their high kinetic energy. Low temperature and high velocity of particles result in dense coatings free of oxide inclusions [14], [15].

Figure 7 depicts the process of cold gas spraying. The gas, typically nitrogen or helium is compressed and heated by a heating coil and after entering a convergent-divergent nozzle it expands to reach supersonic velocities. The powder is injected at the rear of the nozzle and accelerated by the supersonic gas stream [2].

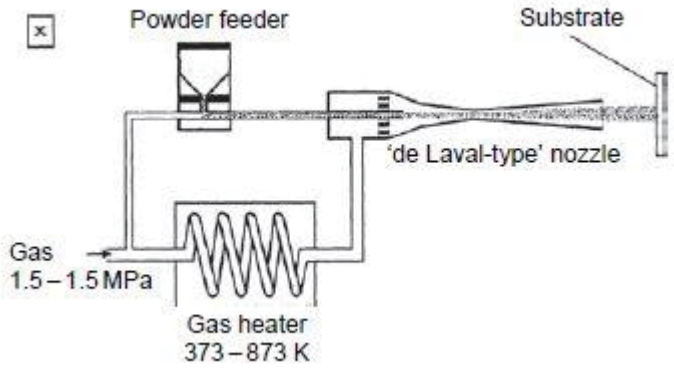

Figure 7. *Schematic of cold spray process [15]*

The structure of a typical thermal spray coating has a lamellar splat structure containing unmelted particles, pores and oxide inclusions as shown in Figure 8. The basic building block is the splat, a single particle or droplet that impacts and adheres to the substrate. The initially sprayed spherical particle deforms and spreads when impacting to the surface, flattening in the process. In this way, the overlapping of splats builds the coating layers showing a lamellar structure [21], [22] .

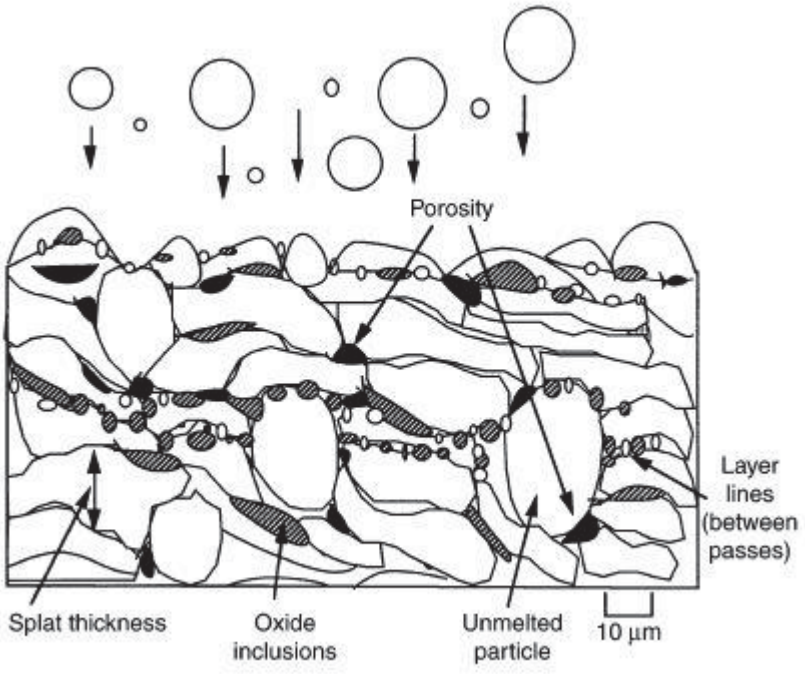

Figure 8. *Thermal spray coating microstructure [21].*

However, like it was mentioned before, the lamellar splat structure is not the only feature within the coating. The degree of particle melting in flight along with the material used, determines the amount of unmelted particles, porosity and oxide stringers. Unmelted particles are those presenting a solid state which could not deform and flatten and thus, they

preserve a spherical shape in the coating layer, interrupting the lamellar structure [21], [19].

Oxide inclusions are produced in metallic coatings by the interaction between hot particles and the atmosphere, creating an oxidation film on the droplet surface. When the droplet impacts the surface, the oxidation film fractures and flows with the metal adhering to the coating layer. They are also called oxide stringers because of their characterised elongated shape, similar to a string. The presence of oxide inclusions increases coating hardness and it can lead to brittleness and thus fracture of the layer. Besides, inclusions decrease cohesive strength due to their interference with the splats. This is why oxidation is usually undesirable, although there are some applications where oxide stringers are beneficial, such as those in which high wear resistance or lower thermal conductivity are needed [21], [19].

In order to minimize oxide inclusions, which are usually a detrimental feature, some process parameters can be modified. Removing the reacting environment using inert gases or chambers, like it is done in vacuum plasma spraying, would avoid the interactions between particles and the atmosphere. Lowering the heat capacity of the equipment, as in cold kinetic spraying, reduces the average temperature of droplets. The particles dwell time should be decreased by minimising spray distances or increasing velocities and the temperature of the substrate should be reduced as well by using cooling jets or increasing the speed of the thermal spray device across the surface. Finally, the particle size is not a trivial parameter since larger droplets have lower specific area, which minimizes the overall oxide content [21], [19].

Porosity is another characteristic that determines coating properties. As for oxide inclusions, it is not a desired feature although it is beneficial in some applications such as medical implants, in which interfacial bond between material and tissue is enhanced with the presence of pores. The majority of applications try to avoid porosity because it decreases cohesion strength between splats and reduces wear and corrosion resistance [21], [19].

Porosity has multiple origins, like material shrinkage when cooling from the liquid state. Since the cooling is not homogenous, some areas shrink faster than others creating pores in the process. Another porosity origin is the presence of unmelted or resolidified particles that interrupt the lamellar splat structure creating voids. Poor cohesion and intersplat or intrasplat cracking leads to porosity as well. In addition, the feedstock powders have their own inherent pores. Other sources of porosity, shown in Figure 9 and Figure 10, are shadowing and masking. The shadowing effect is produced when the angle of the spray is below 45˚ in which the unmelted particles create voids that are not filled by the droplets. Masking is related to corner radius or edges that contribute to localised porosity [21], [19].

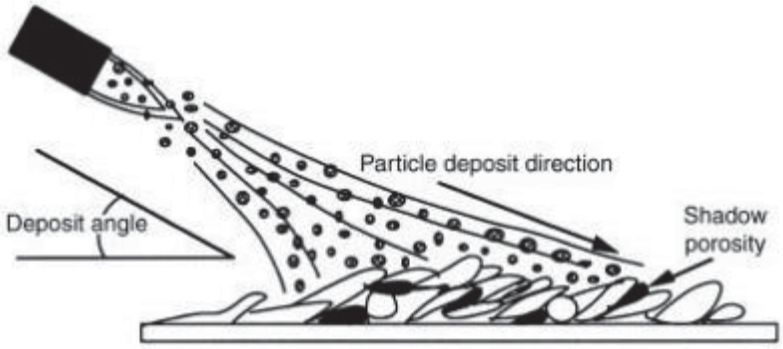

Figure 9. *Porosity created by shadowing [21].*

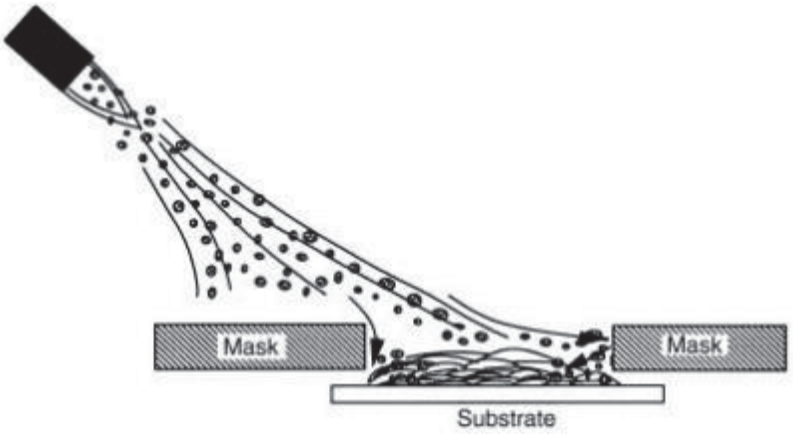

Figure 10. *Porosity created by masking interference [21].*

As it has been seen, the feedstock material, the chosen technology and the parameters used during spraying will determine the structure and hence the final properties of the coating. In the following subsections HVOF and HVAF processes are described with more detail.

2.3 HVOF process and coatings

HVOF is a thermal spraying process whose heat source is based on the chemical energy of gas combustion, as was mentioned before. This process was invented in 1958 by Union Carbide (now Praxair Surface Technologies) as a derivative of D-gun with the difference of burning the fuel in a continuous way. However, it was not until the early 1980s that it gained commercial acceptance, when James Browning introduced the Jet-Kote system as an effort to compete with D-gun coatings [15], [17].

As shown in Figure 11, in the gas or liquid fuel HVOF process the fuel is introduced with oxygen into the combustion chamber, where the ignition will provoke combustion and

the exhaust gases will pass through the nozzle and barrel dragging and propelling the powder towards the substrate. Depending on the torch design, powder is introduced axially or radially into the jet [15].

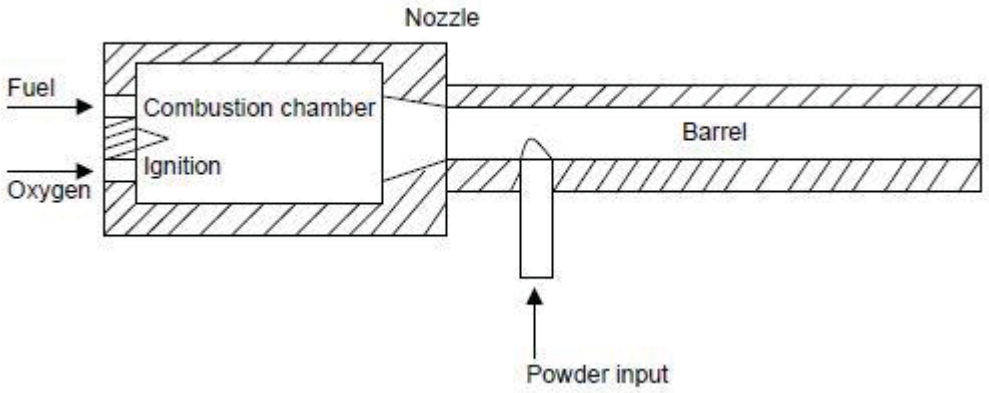

Figure 11. *Schematic of a HVOF torch [15].*

The common coatings deposited with the HVOF process are cermet coatings of tungsten carbide or chromium carbide as the hard phase embedded in a ductile metal matrix. Typical coating systems are WC–Co, WC–CoCr, WC–NiCr or Cr_3C_2-NiCr. In addition, HVOF sprayed metallic coatings have found many uses, e.g. MCrAlY, where M can be iron, nickel, and/or cobalt, are applied in aircraft turbine blades for their high temperature resistance [17], [23].

HVOF coatings are used for several wear and corrosion applications in mining, pulp and paper processing, aerospace and automotive manufacturing, electric power generation or petrochemical industry. Examples of wear types resisted by the HVOF coatings are abrasion, slurry erosion, cavitation erosion, sliding-wear or solid particle erosion. In the aerospace, automotive and marine industry, HVOF coatings are applied as an alternative to hard chrome plating, a process that uses hexavalent chromium which presents adverse health and environmental effects [1], [24]-[28].

There are different designs of HVOF torches, in which the location of powder injection, the type of fuel, the water cooling amount and the design of the combustion chamber, the burner and the exit nozzle geometry can vary significantly. The following Figure 12 and Figure 13 describe two different torch designs that use gaseous fuel and liquid fuel, respectively [29].

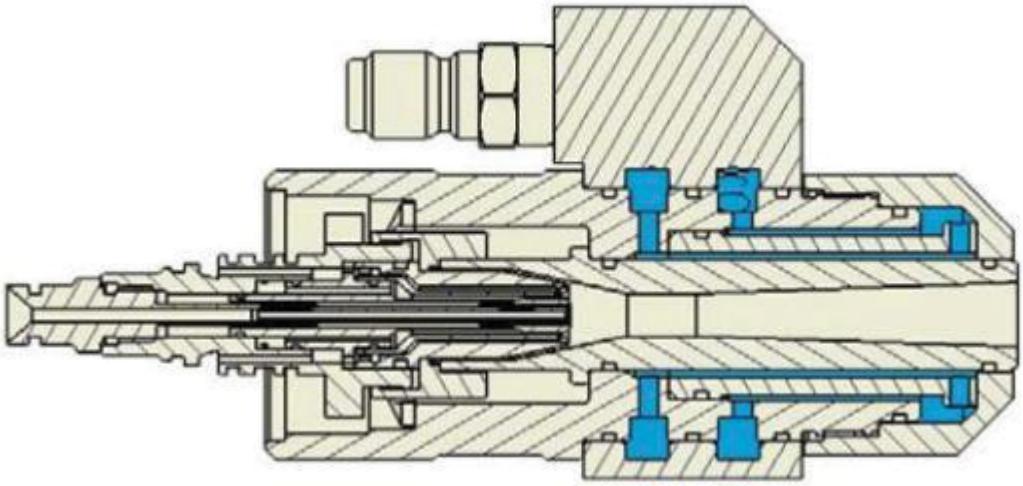

Figure 12. *Cross-section of the DJ2700 torch [29].*

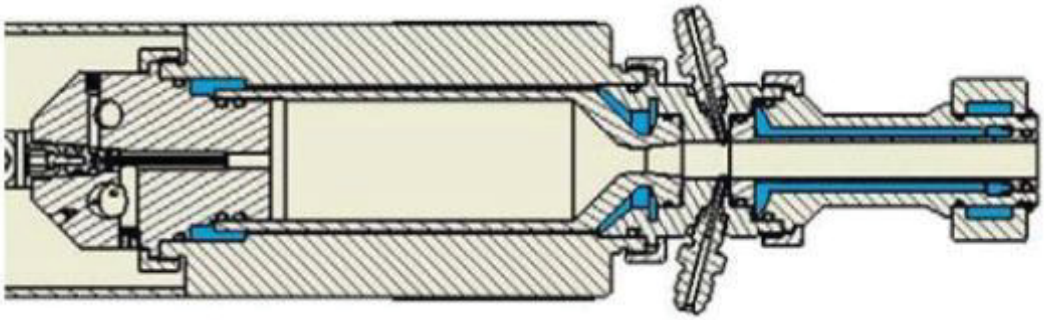

Figure 13. *Cross-section of the JP-5000 torch [29].*

The Diamond Jet torch in Figure 12 is fed with gas fuel and it has two basic configurations that have different cooling systems. The air cooled configuration, like the DJ2600 torch, has a converging-cylindrical nozzle that limits the gas stream velocities. The hybrid configuration, like the DJH2700 torch, uses a combination of air and water cooling and has a convergent-divergent nozzle that allows higher gas velocities than in the conventional configuration. For both designs, powder is injected axially to the combustion chamber and the possible fuels to use are hydrogen, methane, ethylene, propylene and propane [29].

The JP-5000 torch is fuelled with kerosene and its exhaust gases leave the combustion chamber through a converging-diverging nozzle attached to a straight duct. Similar to the hybrid configuration of the Diamond Jet torches, JP-5000 is water cooled as well. However, powder injection is done radially after the nozzle throat into the expanding gas stream causing a lower particle temperature. Moreover, due to the use of kerosene a longer combustion chamber is needed to enhance the mixing of oxygen with fuel, which

presents a large droplet size, and to avoid carbon buildup in the chamber produced by unburned products [29].

Talking about thermal efficiency, JP-5000 has greater thermal losses transferred to the water cooling system than the Diamond Jet torches. This fact is caused by the higher surface of the JP-5000 combustion chamber. While the propane fuelled DJH2700 torch presents a thermal efficiency of 95%, the kerosene fuelled JP-5000 has only 74%, which means that 26% of the heat input is transferred into the cooling water [29].

Regarding the energy input, JP-5000 torches need twice the amount of heat input than the Diamond Jet. The reasons are the powder injection downstream of the combustion chamber and the lower thermal efficiency of the kerosene fuelled torch. Gas temperature has its highest value at the combustion chamber and it decreased substantially after the nozzle exit, then in order to melt the powder in the JP-5000 torch a higher heat input is needed. Moreover, a quarter of this heat input is transferred to cooling water [29].

Curves shown in Figure 14 were obtained by Rusch [29] using compressible fluid equations assuming 2700ºK of combustion temperature and 1 atmosphere of exit pressure. Curves for propane, propylene, acetylene and ethylene are similar to that of hydrogen. Looking at the figure, it can be seen that gas velocity depends on the fuel used and the combustion chamber pressure. The slope gets lower when increasing combustion chamber pressure, which means that HVOF technology is limited to gas velocities of 1900 to 2200 m/s due to technical and economic reasons.

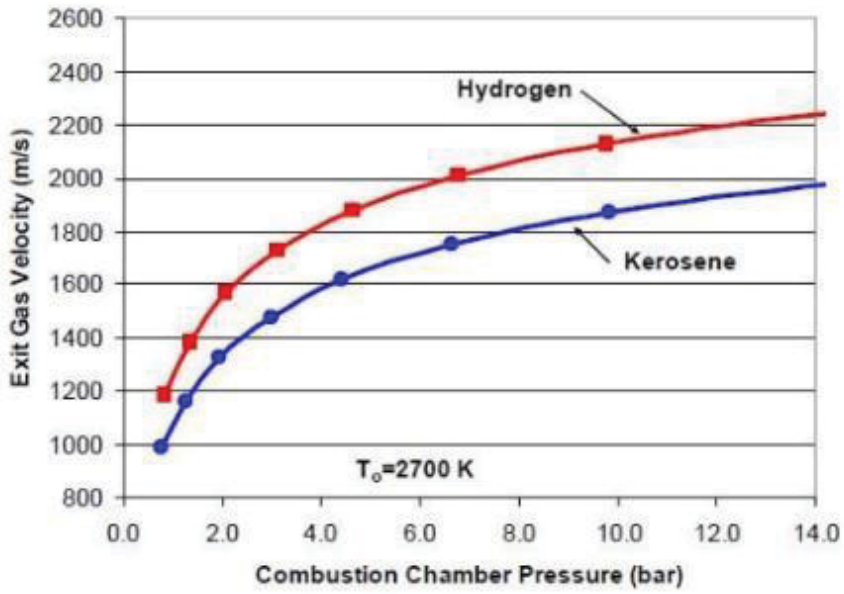

Figure 14. *Influence of combustion chamber pressure on exit gas velocity [29].*

Table 1 presents important properties of HVOF fuels such as maximum flame temperature, heat of combustion and oxygen-fuel ratio. Acetylene shows the highest maximum flame temperature, a parameter that can be easily adjusted by the oxygen-fuel ratio [14].

Table 1. *Properties of different fuels used in HVOF torches [30].*

Fuel	Maximum flame temperature (°C)	Heat of combustion (MJm^{-3})	Oxygen-fuel ratio for HVOF applications
Propane	2828	93.2	3.0-8.0
Propylene	2896	87.6	3.5-7.0
Hydrogen	2856	10.8	0.3-0.6
Ethylene	2924	59.5	2.0-5.0
Acetylene	3160	56.4	1.3-4.0
Kerosene	2900	37.3 MJL^{-1}	2.8-4.8

2.4 HVAF process and coatings

The HVAF process was presented in the early 1990s by Browning [31] to exploit the engineering theory of hypervelocity impact fusion. According to this theory, the powder injected to a nozzle is accelerated to extreme velocities by a hot supersonic gas stream whose temperature is below the melting point of the particles. The high kinetic energy is converted to thermal energy at the moment of the impact, allowing particles to melt and deform in the substrate. This principle is used in cold spraying as well but with the difference of generating the hot gas stream by electrical heating instead of combustion [32], [33].

HVAF process is similar to HVOF, but it is using compressed air as the oxidizer. The operating costs of this process decrease since pure oxygen is more expensive than air and besides, security expenses are lower due to the safer and more controllable combustion.

The first commercial system, AeroSpray, was a kerosene fuelled torch based on patents of Browning [31], [34]. Similar to the liquid fuel HVOF gun, AeroSpray had a large combustion chamber to obtain a good air-kerosene mixture and powder was injected radially in the expanded nozzle section. Activated combustion (AC) HVAF torches are modern commercial spray equipment designed by Uniquecoat Technologies and Kermetico. AC-HVAF uses gaseous fuel and a catalytic ceramic insert that after the initial combustion heats up the fuel-air mixture over the auto-ignition temperature allowing the reduction of combustion chamber size and axial powder injection. Figure 15 shows an illustration of a modern gaseous fuel HVAF torch, in which a second mixture of air and fuel is introduced in the nozzle to propel the powder. This HVAF equipment achieves particle velocities well above previous HVAF torches that result in dense coatings with low oxidation due to the low particle temperature [14], [35].

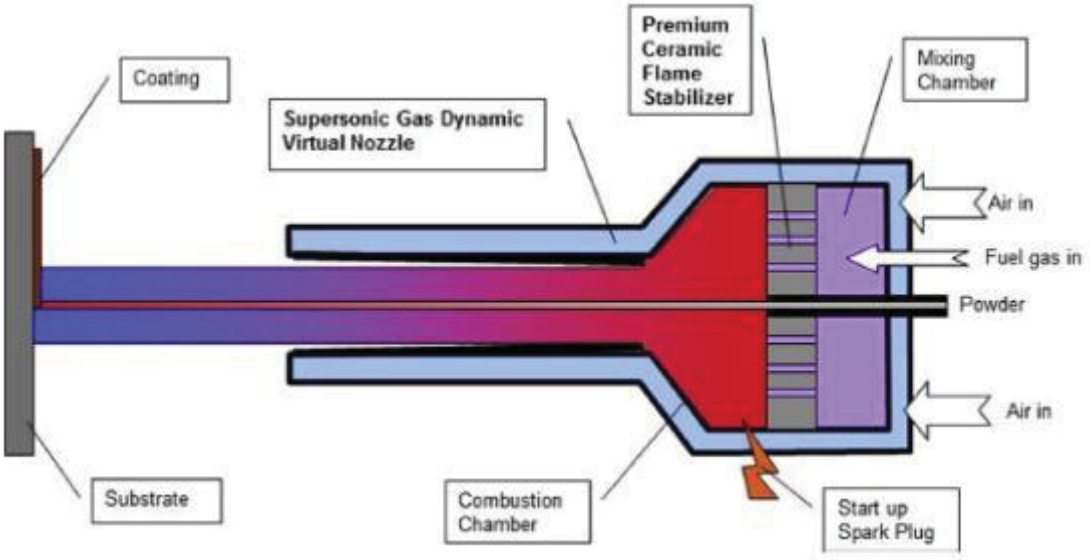

Figure 15. *Illustration of a modern HVAF torch (M3) [14].*

Figure 16 shows the influence of the oxygen-fuel ratio on the flame temperature for different gas and liquid mixtures. HVOF spraying that mixes fuel with oxygen presents for a stoichiometric combustion a flame temperature ranging from 2700 to 3000 ºC being the lowest value for kerosene and the highest for acetylene. On the other hand, the mixture of kerosene and air, used by a HVAF torch, presents a flame temperature of 2000 ºC. This decrease in flame temperature produces coatings with reduced oxidation and with lower amounts of dissolved carbides in the case of WC-Co (Cr) coatings [14].

Better wear performance has been reported for HVAF coatings in the literature. For instance, in WC-cermet coatings sprayed with liquid fuel HVAF, Jacobs *et al.* [1] observes an improvement of HVAF coatings over HVOF coatings in sliding-wear performance explained by the retention of WC particles and the absence of brittle W_2C in the HVAF

process. Moreover, average hardness is found higher for HVAF coatings which present a fine and dispersed microstructure in comparison to HVOF coatings that show segregation with large metallic phase areas [2]. Absence of carbide dissolution in the HVAF process against the decarburization of the sprayed HVOF coatings was concluded as well by Wang et al. [3].

Next, cavitation and slurry erosion are defined and the apparatus used to test the effect of these phenomena are described as well.

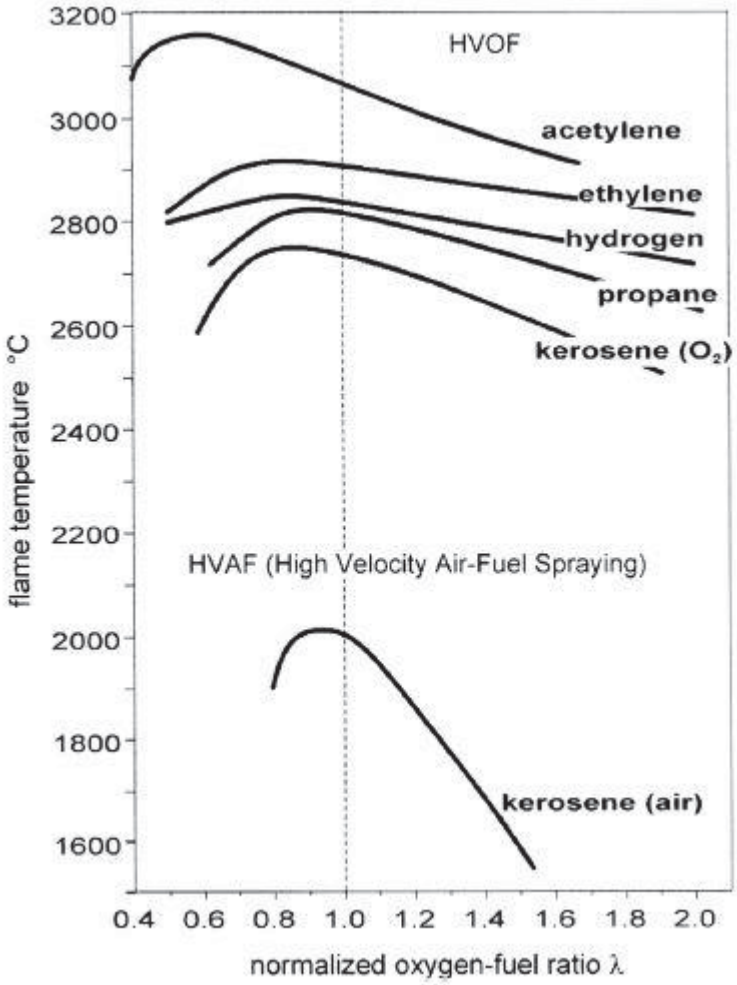

Figure 16. *Influence of oxygen-fuel ratio on flame temperature [30].*

2.5 Cavitation and slurry erosion

Cavitation is the phenomenon of formation and subsequent collapse of bubbles that contain vapour or a mixture of vapour and gas that occur on a solid surface in contact with a liquid. Bubbles are formed in those areas with negative or near-zero pressure, for instance when a flow of liquid enters a diverging geometry. Then, when bubbles or cavities are

submitted to a higher pressure near a solid surface, they collapse violently creating micro-jets of liquid accelerated towards the surface. These shock waves generate large stresses that damage the solid. Figure 17 shows the mechanism of cavitation erosion wear [26], [36], [37].

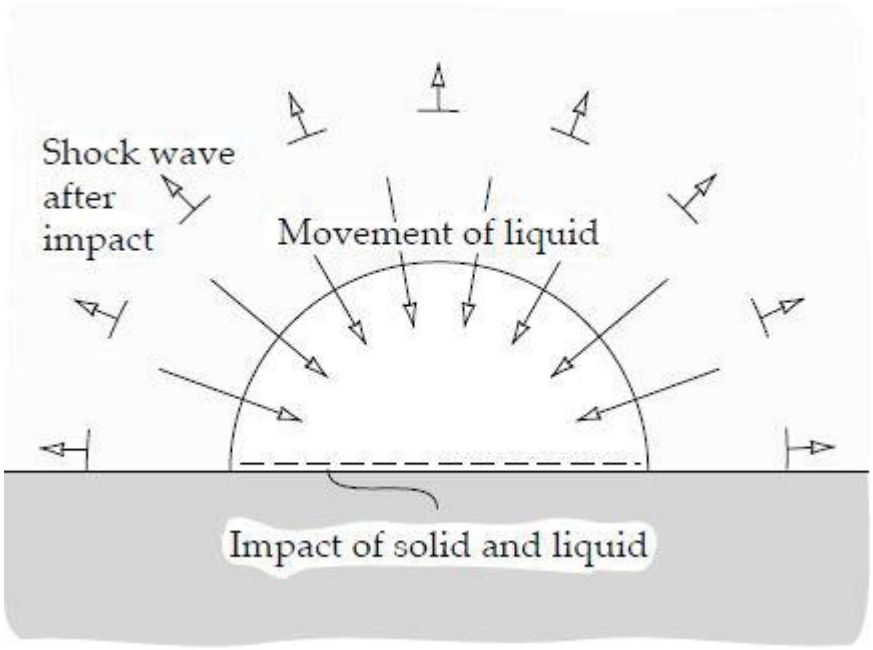

Figure 17. *Mechanism of bubble collapse [37].*

The stresses caused by cavitation lead to formation of holes or craters that further increase the wear rate ending with the destruction of the affected component. Cavitation erosion is common in hydraulic components such as valves, pipelines, pumps, water-turbine blades or diesel engines which can eventually failure. In order to reduce cavitation damage, HVOF coatings have been reported to improve wear, corrosion and fatigue resistance of the substrate. Mass loss was observed to begin at the edge of pores, the interface of unmelted or half-melted particles and the matrix and the interface of different phases [38], [39].

One of the most common cavitation test rig consists of a vibratory apparatus whose specifications can be found in the ASTM G32 standard. This test method is further described in the cavitation erosion test section 3.1. Other methods include Venturi, rotating discs and jet impingement rigs. The Venturi effect that occurs when a fluid flows through a constricted section is used to induce a negative pressure that results in cavitation. Figure 18 shows the cavitation cloud generated at the Venturi section of a high speed closed-loop cavitation tunnel [36], [40].

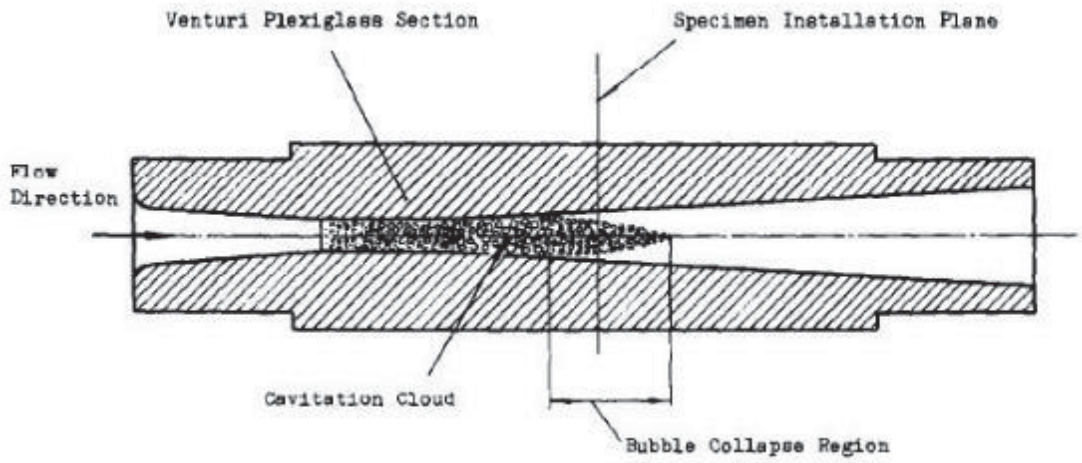

Figure 18. *Venturi test section [40].*

Figure 19 shows a rotating disc apparatus that consists of a test chamber in which a disc is rotated in water with samples mounted in grooves. The source of cavity formation in the water are the inducers placed next to the grooves. In this configuration, cavities collapsed approximately at the centre of the test sample. On the other hand, a jet impingement tester is presented in Figure 20, in which specimens are fixed to the periphery of a rotating disc inside a chamber and two water jets impinge on them to cause cavitation erosion [41], [42].

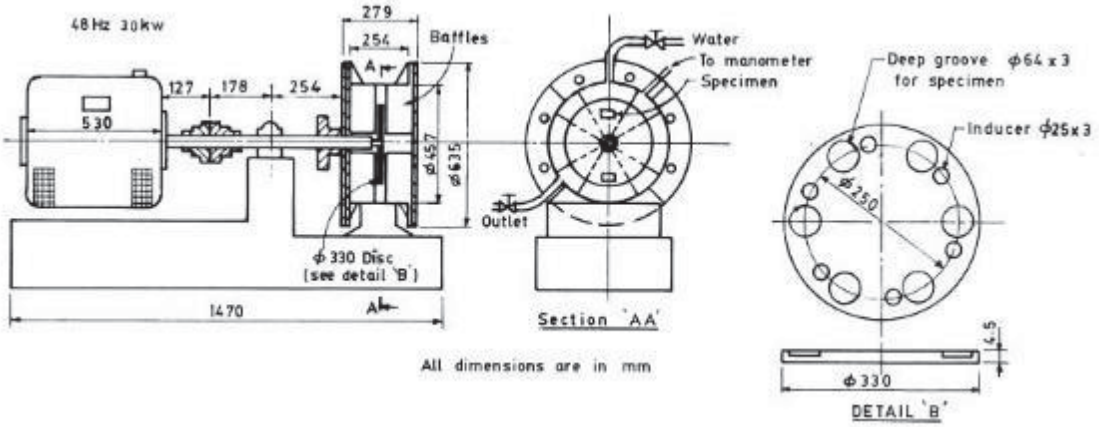

Figure 19. *Rotating disc apparatus [41].*

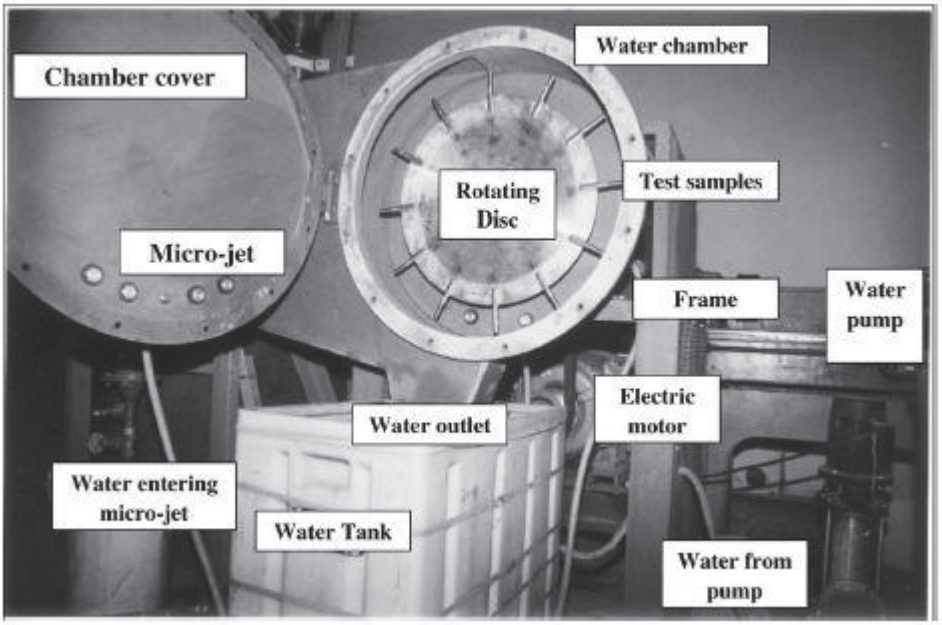

Figure 20. *Water jet impingement erosion test facility [42].*

Slurry erosion, on the other hand, is a wear phenomenon caused by solid particles entrained in a liquid medium that impact a component's surface. The continuous impacts on the surface generate large stresses that results in material deformation and mass loss. Slurry erosion is highly severe in hydraulic components like pumps, hydro turbines, propellers, control valves or pipelines which suffer a loss of performance. This phenomenon leads to shut-down of the hydropower plants located in the Himalayan region in India during the monsoon season due to the abrupt increase of solid particles in water, which results in huge economic losses [43]-[47].

Slurry erosion is a type of abrasive wear that is defined by ASTM International as the loss of material due to hard particles that are forced against and move along a solid surface [48]. The main mechanisms of abrasive wear are cutting, fracture, fatigue by repeated ploughing and grain pull-out that are shown in Figure 21.

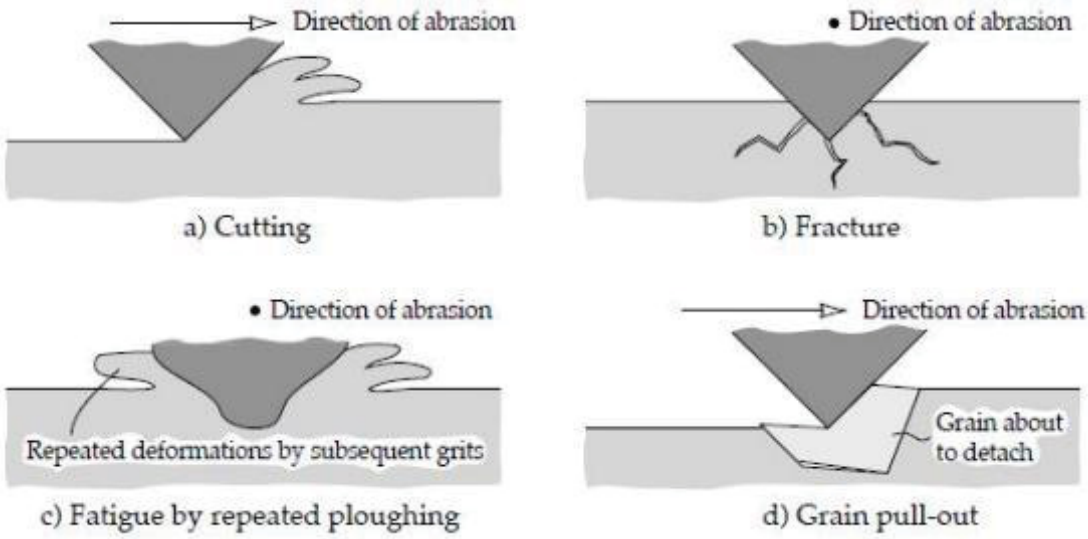

Figure 21. *Mechanisms of abrasive wear [37].*

In the mechanism of cutting, a sharp grit cuts the softer surface removing material as wear debris. Plastic deformation occurs beneath the surface of the abraded material and a subsequent strain hardening can take place which usually results in a reduction of abrasive wear. In the case of brittle materials, fracture can happen due to the impact of a sharp grit against the surface. Formation of cracks and their convergence will result in wear debris as well. On the other hand, when a ductile surface continuously receives the impacts of blunt grits, fatigue occurs with repeated deformations. Finally, grain pull-out is the detachment of an entire grain which had weak boundaries with the surrounding grains. This wear mechanism is found in ceramics [37].

In order to study the effect of slurry erosion, different test apparatus have been designed including the rotatory-type test rigs and the jet-type test. In rotatory-type test rigs specimens are attached to a shaft that rotates immersed in a slurry solution. Slurry pot-testers, the most commonly used rotatory-type test rigs, maintain the slurry solution in the pot and it can be stirred with a mixing fan or with the rotating shaft as shown in Figure 22. Figure 23 presents another design of a rotatory-type tester in which the solution is mixed in a slurry tank that is connected to an erosion chamber with inlet and outlet pipes. In this apparatus the rotation of the shaft in the erosion chamber leads to centrifugal action that forces the slurry to flow out of the chamber and due to the resulting partial vacuum, replacing solution is sucked from the slurry tank. Then, the slurry is recirculated during the test. Disadvantages of the rotatory-tests are the lack of control of variables like velocity, concentration and impingement angle of the slurry and the progressive comminution of the abrasive particles [49]-[51].

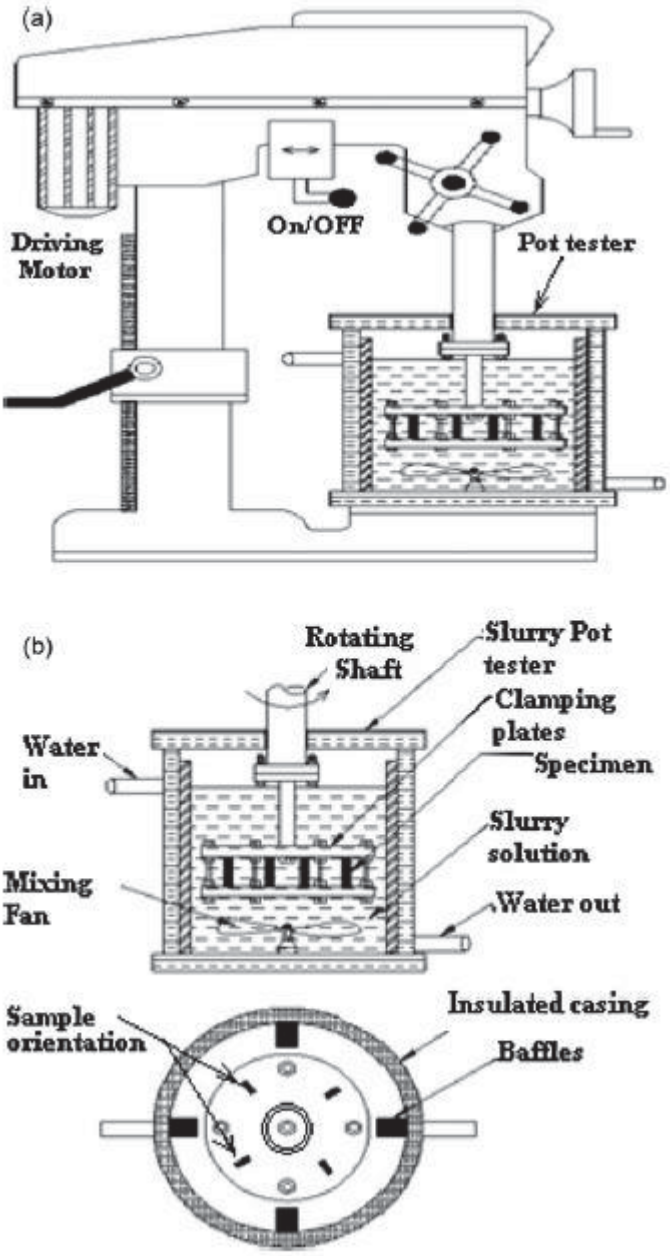

Figure 22. *Schematic of a rotary-pot type test rig: a) General arrangement, b) Pot tester [52].*

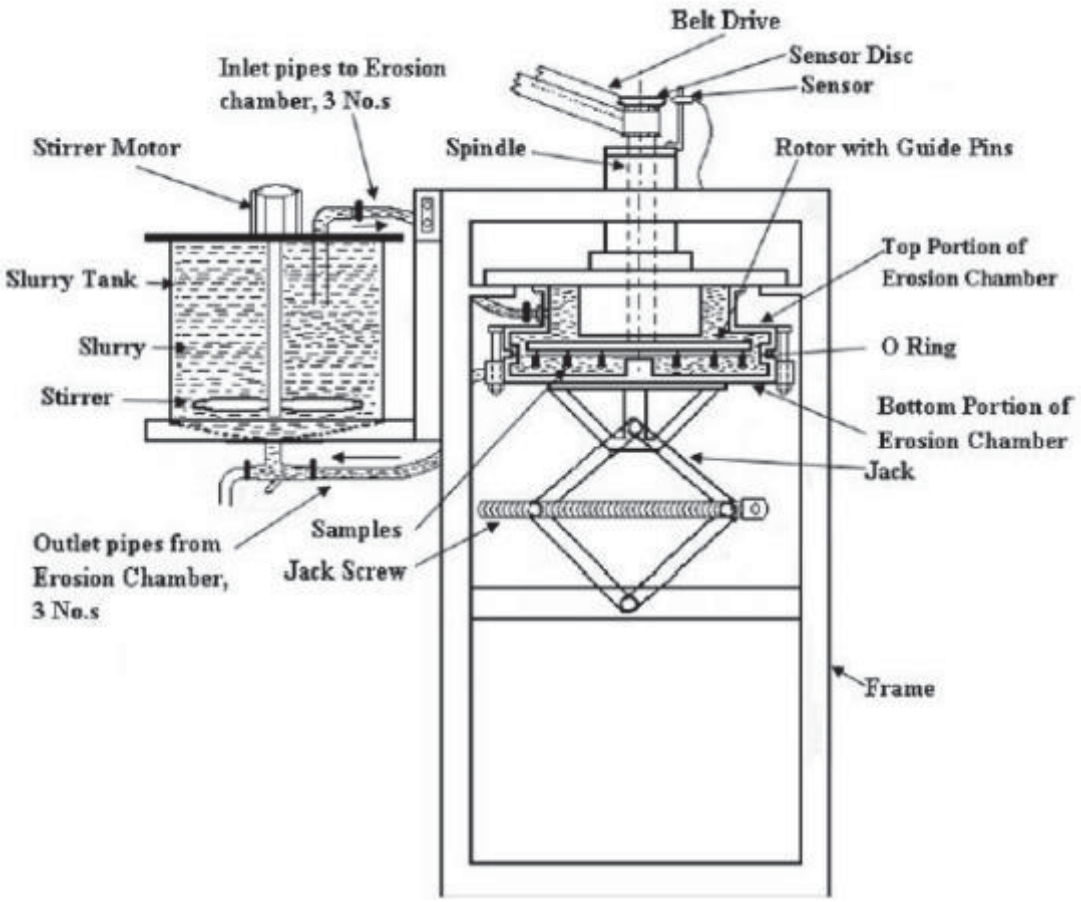

Figure 23. *Schematic of a rotatory centrifugal type tester [45].*

Finer control of parameters such as impact angle and sand concentration is achieved with the jet-type test rigs, shown in Figure 24, Figure 25 and Figure 26, that are based on the ejection of a jet of slurry to impact the sample arranged at a desired angle. However, large viscosity of the slurry avoids getting a high impact velocity and it must be measured periodically due to the wear of the nozzle. There are several kinds of test rigs differing in velocity, sand concentration, sand suction method and if slurry is circulated or not. Among them, closed loop rigs are expensive because of the material loss of pumps and pipes involved in the re-circulation of the slurry. A more economic alternative is the semi recirculating jet-type erosion test designed by Zu et al. [53], in which only water is circulated through the loop system as shown in Figure 25 [24], [49], [50], [54], [55].

Figure 26 presents a whirling arm test rig, another kind of the jet-type test rigs. Here, specimens are fixed at the end of four arms attached to a rotatory shaft and are impacted by a falling slurry stream. The test is carried out in a vacuum chamber to eliminate aerodynamic effects on the slurry stream. Before entering the slurry into the vacuum chamber, a tank mixes the solution that will be fed to a stabilizing funnel so as to obtain a homogenous mixture with no solid accumulations at the entrance of the orifice [50], [56].

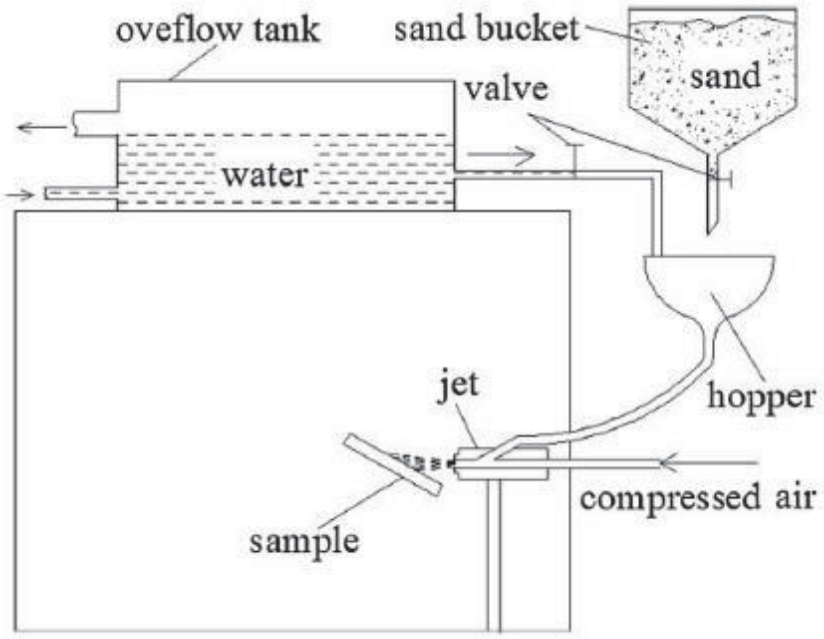

Figure 24. *Schematic of a non-recirculating jet-type test rig [57].*

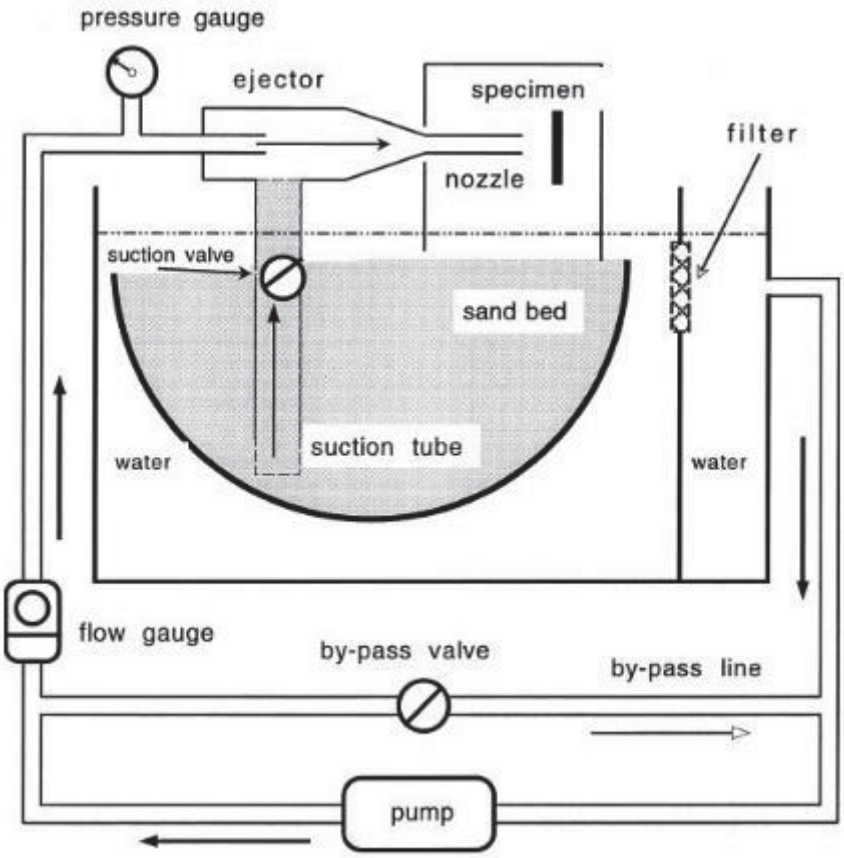

Figure 25. *Schematic of a semi recirculating jet-type test rig [54].*

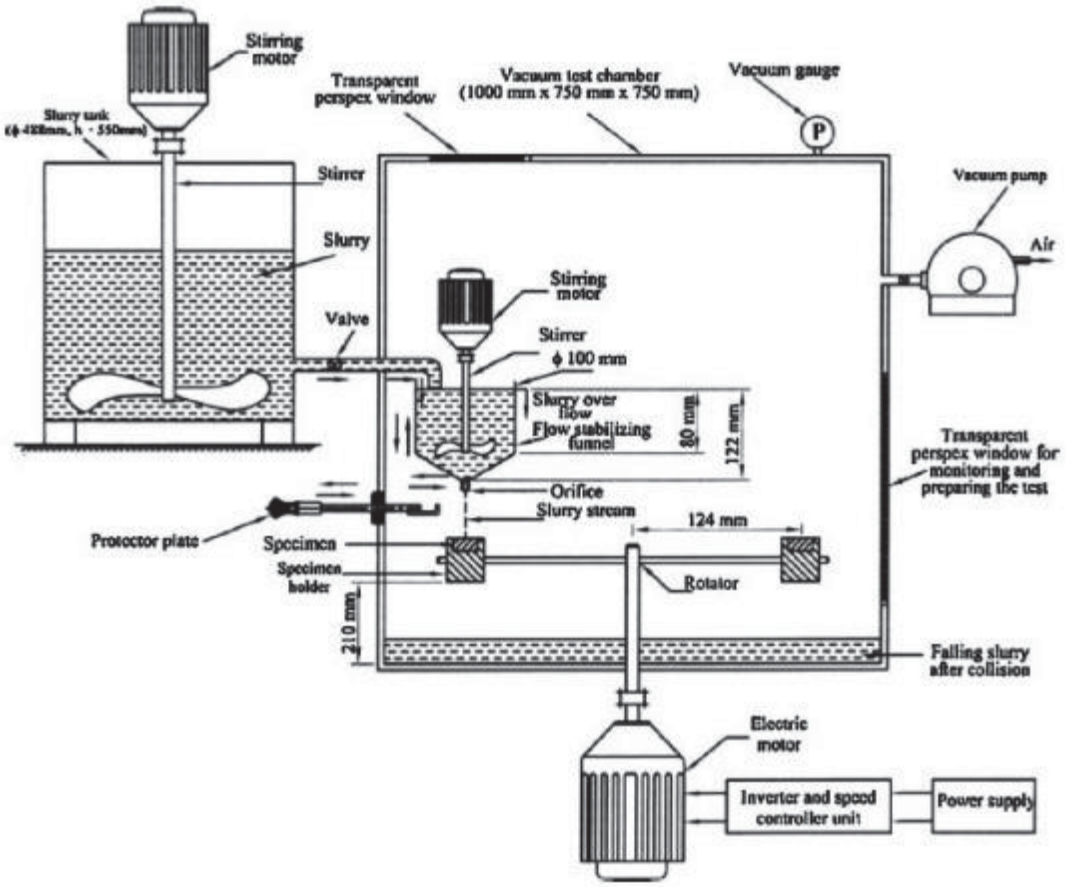

Figure 26. *Schematic of a whirling arm test rig [50].*

Regardless of the test type used, slurry erosion will depend on factors such as average size and shape of abrasives, impact velocity and slurry concentration. Bigger particle size increases erosion rates due to the increase of kinetic energy and irregular particles with sharp edges will be more abrasive than blunt ones [37], [45]. Erosion increases also with impact velocity since wear occurs as a result of relative motion between the erodent and the target surface, a fact proved by many researchers [58]-[61]. Talking about the impingement angle, ductile materials will present bigger mass loss at angles between 20 and 30º while brittle materials will undergo maximum erosion at 90º. Finally, an increase in erodent concentration initially increases slurry erosion because of increase in number of the impact events. However, increase in slurry concentration beyond a threshold value causes a shielding phenomenon that consists in the interaction between the incoming and the rebounded particles leading to a reduction in the impact velocity and therefore a decrease in the erosion rate [43].

3. RESEARCH METHODOLOGY AND MATERIALS

In this section the research methodology and the materials used will be explained.

As it has been mentioned before, two kinds of hardmetals were tested: Cr_3C_2-25NiCr and WC-10Co4Cr. These hardmetal coatings were thermally sprayed with gas fuel HVOF, liquid fuel HVOF and HVAF spray processes. Two separate feedstock powders were used for both chemical compositions, WC-10Co4Cr and Cr_3C_2-25NiCr. Therefore, four coatings were produced with each of the three processes resulting in twelve different material/process combinations. The details of the twelve studied coatings and their designations are shown in Table 2.

All the powders were agglomerated and sintered except for the Cr_3C_2-25NiCr ones from Oerlikon Metco, which apart from being agglomerated and sintered, were also plasma densified. According to Berndt [62], this process of plasma densification results in spherical particles with higher strength and density, meaning a higher resistance against breakage during the spraying. It can be noticed that a smaller particle size distribution was used for HVAF spraying. The reason is the lower working temperature of the process that would not be able to provide sufficient melting of bigger particles.

The coatings were sprayed on AISI 316L stainless steel substrates that were grit blasted prior to spraying to clean the surface and provide increased surface roughness for mechanical bonding of the coating. The same stainless steel material would be used uncoated as reference samples for both cavitation and slurry erosion tests.

Before testing the samples, they were prepared with diamond grinding disks with varying grit sizes. For grit sizes, ISO/FEPA grit designation is used, e.g. P220, P500 and P1200. Polishing was done with 3 µm diamond suspension and cloth disc.

Once the tests were performed, whose methodology and equipment is described in the following subsections, the mass loss was measured. However, for the results analysis volume loss would be use instead of mass loss. For this purpose, the theoretical densities of Cr_3C_2-25NiCr and WC-10Co4Cr were calculated as described below.

WC-10Co4Cr alloy presents 86% of tungsten carbide (WC), 10% of cobalt (Co) and 4% of chromium (Cr), all percentages referring to weight. Cr_3C_2-25NiCr is constituted of 75% of chromium carbide (Cr_3C_2), 20% of nickel (Ni) and 5% of chromium (Cr) [7], [63]. Taking into account the real density of each element and compound, the alloy density is easy to calculate as shown in the equation.

Table 2. *Details of the sprayed coatings and feedstock powders.*

Sample code	Process	Chemical composition	Manufacturer	Particle size [µm]
C1DJ	DJH2700	Cr_3C_2-25NiCr	H.C. Starck	-45+15
C2DJ	DJH2700	Cr_3C_2-25NiCr	Oerlikon Metco	-45+15
C1JP	JP-5000	Cr_3C_2-25NiCr	H.C. Starck	-45+15
C2JP	JP-5000	Cr_3C_2-25NiCr	Oerlikon Metco	-30+10
C1M3	M3	Cr_3C_2-25NiCr	H.C. Starck	-30+5
C2M3	M3	Cr_3C_2-25NiCr	Oerlikon Metco	-30+10
W1DJ	DJH2700	WC-10Co4Cr	H.C. Starck	-45+15
W2DJ	DJH2700	WC-10Co4Cr	Durum	-36+15
W1JP	JP-5000	WC-10Co4Cr	H.C. Starck	-45+15
W2JP	JP-5000	WC-10Co4Cr	Durum	-36+15
W1M3	M3	WC-10Co4Cr	H.C. Starck	-30+5
W2M3	M3	WC-10Co4Cr	Durum	-25+5

$$\rho_{alloy} = \frac{100}{\sum_{i=1}^{n} \frac{w_i}{\rho_i}} \; [g/cm^3]$$

Where ρ_{alloy} is the real density of the alloy, w_i is the weight percentage of each element or compound, ρ_i is the real density of each element or compound and i refers to the different elements and compounds that constitute the alloy. The calculated densities are presented in 0.

Table 3. *Real densities of alloys and elements and compounds present in the alloys*

Element/compound/alloy	**Cr**	**Co**	**Ni**	**Cr_3C_2**	**WC**	**Cr_3C_2-25NiCr**	**WC-10Co4Cr**
Density (g/cm^3)	7.19	8.9	8.9	6.68	15.7	7.05	13.97

The microstructure and morphology of the polished coatings and their wear surfaces were observed before and after the tests by scanning electron microscope (SEM, XL-30, Philips, Netherlands). Secondary electron (SE) and backscattered electron (BSE) images were taken. SE images are built from the collection of secondary electrons, which are loosely bound electrons released from the sample after interacting with the SEM electron beam. The intensity of the signal depends on the angle between the incident beam and the specimen surface, which makes SE images especially useful for topographical analysis. On the other hand, BSE images are based on beam electrons that are scattered elastically from the sample. The BSE signal depends on the atomic number of the specimen and higher atomic numbers lead to higher quantity of scattered electrons, which produces brighter areas in BSE micrographs. This phenomenon is useful when analysing polished samples, because the atomic number contrast shows the different chemical compositions and phases in the specimen [64].

3.1 Cavitation erosion test

The cavitation erosion test was performed following the ASTM G32 standard and using the modified test method with stationary sample [36]. The standard guidelines were followed and a vibratory apparatus as shown in Figure 27 was used. The dimensions of the samples used for the cavitation tests were 25x25x5 mm^3.

Vibrations are generated by a transducer connected to a generator. The transducer is attached to a horn or velocity transformer in order to obtain a higher vibratory amplitude at the sample than at the transducer. The test specimen was submerged in approximately 1 litre of distilled water contained in a beaker and the sample was fixed to an attachment with four screws. The temperature of the water was maintained at 25 ± 1 ºC throughout

the test by a cooling coil connected to a temperature controller. The oscillation frequency was set to 20 KHz with an amplitude of 50 μm and the distance between the horn tip and the sample surface was set to 0.5 ± 0.1 mm.

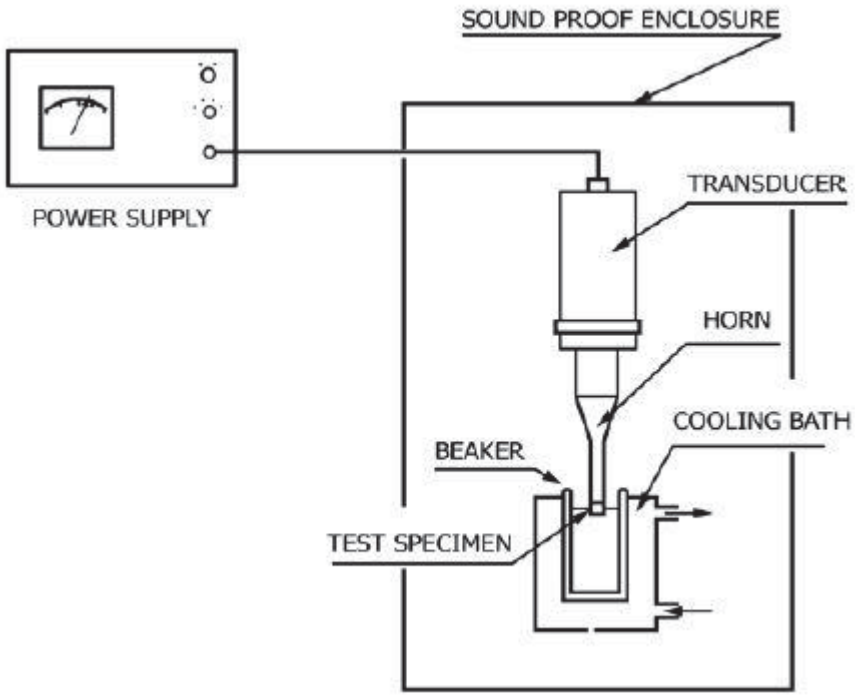

Figure 27. *Schematic of vibratory cavitation erosion apparatus [36].*

Before starting the test, samples were ultrasonically cleaned with ethanol, dried in hot air and weighed with an electronic balance with a sensitivity of 0.1 mg. Then, specimens were tested for 8 hours, measuring the new weight at intervals of 2 hours in which samples would be removed and cleaned in ultrasonic bath before the weighting. Distilled water was changed before executing a new test. In this way, the weight loss produced during the exposure time is reported and then expressed in volume loss as it has been explained before. In addition, mean depth of erosion was calculated as the slope of the volume loss-exposure time graph divided by the tip area which was 188.9 mm^2. The equipment used for the cavitation tests is shown in Figure 28.

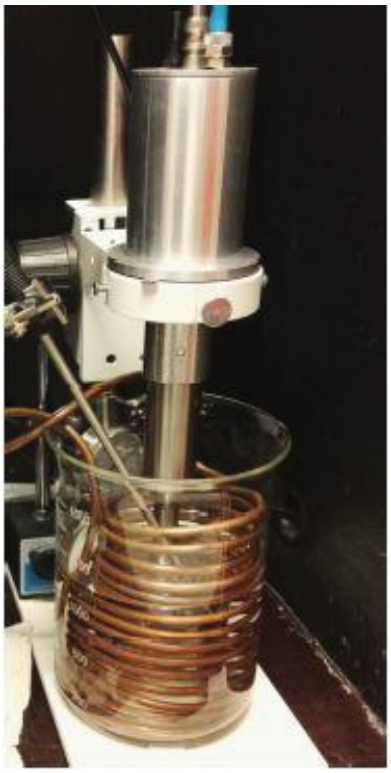

Figure 28. *Cavitation test equipment [65]*

3.2 Slurry erosion test

The slurry erosion tests were performed with a pin mill slurry pot unit shown in Figure 29. This unit is composed of a rotating shaft that submerges into a pot where the slurry is deposited. The dimension of the samples used for the slurry erosion test were 35x35x5 mm^3. The samples were attached to the rotating shaft with similar sample holders as are shown in Figure 29c. This shaft is driven by a motor capable of delivering 1750 rpm with eight mounted square samples at 90° angle. Figure 29b shows the presence of fins inside the pot that are used to avoid the accumulation of erodent particles next to the walls. Cooling of the slurry pot is done by a cooling coil that surrounds it. The temperature was monitored at any time during the test with a thermoelement placed behind one of the fins [51].

For each test run, eight samples in total were attached on four different levels as every level has a place for two samples. However, the slurry concentration differs depending on the level and therefore the wear rate also varies depending on the sample location (level). In order to correct this variation, samples are rotated through all the levels during the test so that eventually all the test specimens have been tested in equal conditions [51].

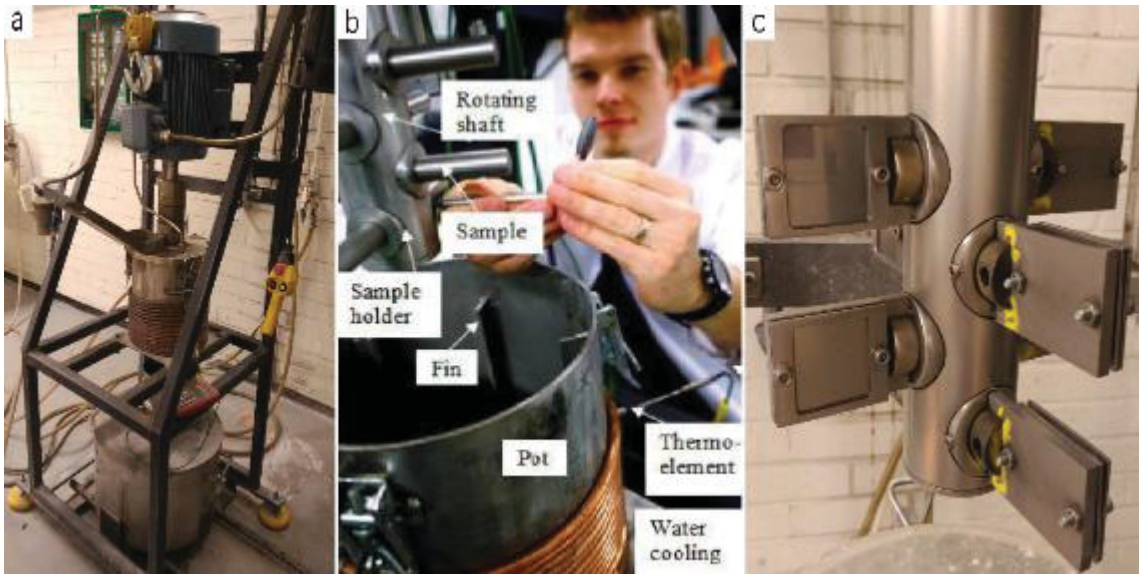

Figure 29. *a) Pin mill slurry pot unit [51], b) Slurry pot elements description [51], c) Sample holders used in the present study.*

The slurry was composed of 10 litres of water and 5 kg of quartz, i.e. 33% of solid content, the speed of the shaft was set to 1200 rpm and the test lasted 80 minutes in total, changing the location of samples every 20 minutes. The slurry was replaced after each 20 min test cycle.

Tests were performed with two different quartz sizes in order to see the effect of the erodent particle size on the wear rate. The chosen particle size distributions were 0.1-0.6 mm and 2-3 mm. Other test parameters were kept constant for both particle sizes. The first test runs with the 0.1-0.6 mm quartz size were weighed with an electronic balance with a sensitivity of 1 mg, while samples tested with the 2-3 quartz size were weighed in a balance with 0.1 mg of sensitivity. The sensitivity of the balance used for the samples tested with fine particles was found to be insufficient for some samples, a fact that must be taken in account when analysing and comparing the results.

4. RESULTS AND ANALYSIS

In this section, results for the cavitation and slurry erosion tests will be presented. These results are micrographs of the wear surfaces and the volume loss experienced by the coatings during the tests. Micrographs of the polished samples are shown as well in the following subsection.

4.1 Characterisation of polished coating surfaces

Before presenting the cavitation and slurry erosion results, polished surfaces for all coatings were analysed. By doing this, it will be easier to explain the main causes of surface wear as the polished coating surface represents the starting condition for both tests. Firstly, the samples coated with Cr_3C_2-25NiCr are described and then the WC-10Co4Cr coatings.

4.1.1 Microstructure of Cr_3C_2-25NiCr coatings

Cr_3C_2-25NiCr samples were analysed by comparing BSE images of the coatings sprayed with the same process but using different powder. The analysis starts with the gas fuel HVOF coatings, followed by liquid fuel HVOF coatings and finally, HVAF samples are presented.

The propane fuelled HVOF coatings C1DJ and C2DJ were sprayed from powders that have the same particle size distribution. The difference lies in the manufacturing process of these powders, since apart from being agglomerated and sintered, plasma densified powder was used for spraying of C2DJ coating. The process of plasma densification results in spherical particles with reduced carbide size and higher strength and density, meaning a higher resistance against breakage during the spraying [62].

The BSE image of C1DJ, in Figure 30a, reveals less and bigger chromium carbide particles than for C2DJ, in Figure 30b, leaving more metal matrix subjected to be removed by quartz cutting. On the other hand, C2DJ presents more carbon dissolution into the metal matrix, noticeable by the grey areas, which could embrittle the coating [1]. Apart from this factors, some damages in form of cracks occurred to C2DJ during the grinding and polishing process. These cracks are pointed out in the image by yellow arrows.

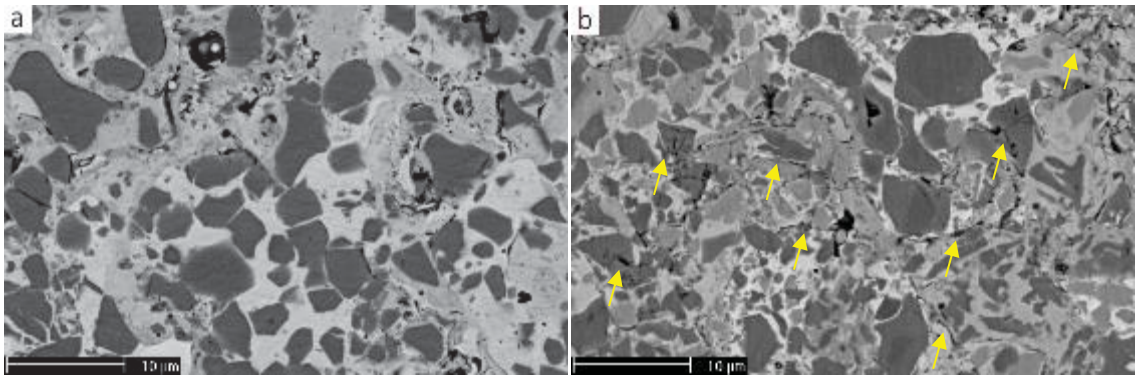

Figure 30. *SEM images of the polished surface microstructue of HVOF sprayed coatings a) C1DJ, b) C2DJ.*

The kerosene fuelled HVOF coatings C1JP and C2JP are shown in Figure 31a and b respectively. The powder manufacturing process is the same as for the gas HVOF coatings, that is to say, C1JP and C2JP were agglomerated and sintered and besides that, the latter one was plasma densified. In this case the particle size distribution is bigger in C1JP and C2JP has a smaller carbide size as a result of plasma densification. There is significant carbon dissolution in C2JP compared to C1JP due to the finer particle size combined with the smaller carbide size. Also, there is much more dissolution even compared to C2DJ because the particle size is smaller in C2JP. Dissolution into the metal matrix may embrittle the coating as it was mentioned above. In the images, some cracks are noticeable in both surfaces marked in yellow arrows.

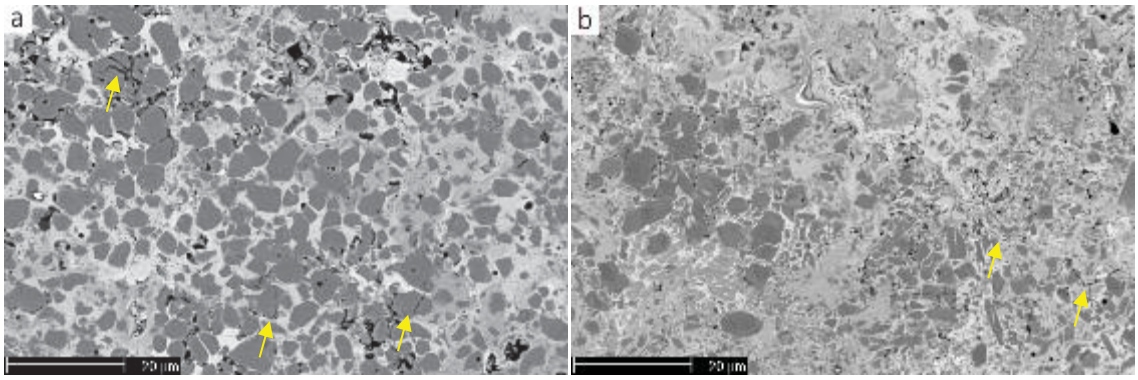

Figure 31. *SEM images of the polished surface microstructure of HVOF sprayed coatings a) C1JP, b) C2JP.*

Finally, the presented HVAF coatings are C1M3 and C2M3, having particle size distributions of -30+5 µm and -30+10 µm respectively. Apart from being agglomerated and sintered, C2M3 powder was plasma densified as well. Looking at the polished surfaces in Figure 32, C1M3 has bigger chromium carbides than C2M3, however, the carbide distribution is not uniform in C1M3, having spots with lesser carbide concentration that are weaker for material removal. Addressing carbon dissolution, higher levels are found in C2M3.

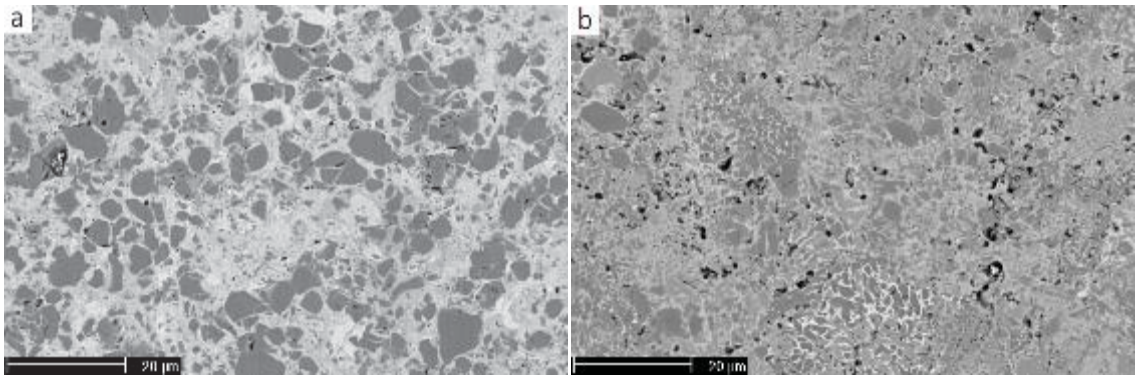

Figure 32. *SEM images of the polished surface microstructure of HVAF sprayed coatings a) C1M3, b) C2M3.*

4.1.2 Microstructure of WC-10Co4Cr coatings

Polished samples of the WC-10Co4Cr coatings are described following the same order of the previous section: gas fuel HVOF coatings are described first, then liquid fuel HVOF samples and finally HVAF coatings.

In these BSE micrographs, unlike Cr_3C_2-25NiCr coatings, carbides have a lighter colour than the metal matrix. This is explained by the molecular weight of tungsten that is higher than that of the cobalt matrix. On the other hand, the powders used in the WC-10Co4Cr coatings were just agglomerated and sintered.

The polished surfaces of the gas fuel HVOF coatings, W1DJ and W2DJ, are shown in Figure 33. The powder particle size distributions were -45+15 for W1DJ and -36+15 for W2DJ. The latter has also a slightly smaller tungsten carbide size. In both coatings there are areas with carbon dissolution into the matrix, which can be seen by the lighter zones in the micrograph. In Figure 33b there are flaws, marked in yellow arrows, which propagate surrounding the carbides without cracking them. These could be the boundaries of the sprayed splats.

The kerosene fuelled HVOF coatings, in Figure 34, are W1JP and W2JP that have the same powder particle size distribution as W1DJ and W2DJ, respectively. Carbide sizes for W1JP are slightly bigger and W2JP presents more areas with carbon dissolution. W2JP has the same type of flaws than in W2DJ, highlighted by yellow arrows, outlining the carbide particles.

Finally, the HVAF coatings, in Figure 35, present the same powder particle distribution. The polished surfaces look similar, same carbide size and no visible cracks. No carbon dissolution is clearly present either.

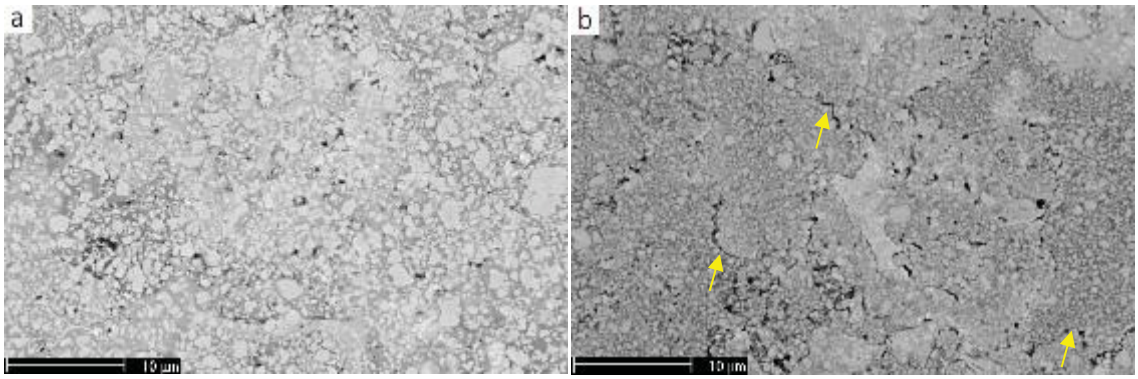

Figure 33. *SEM images of the polished surface microstructure of HVOF sprayed coatings a) W1DJ, b) W2DJ.*

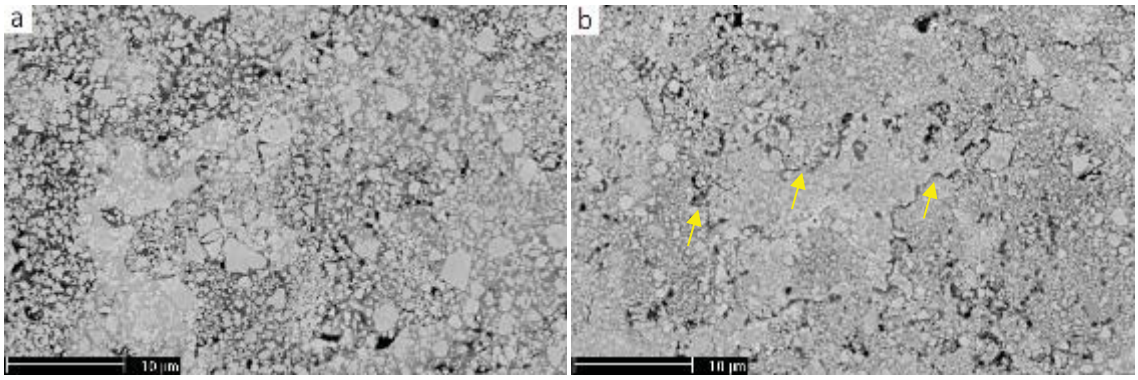

Figure 34. *SEM images of the polished surface microstructure of HVOF sprayed coatings a) W1JP, b) W2JP.*

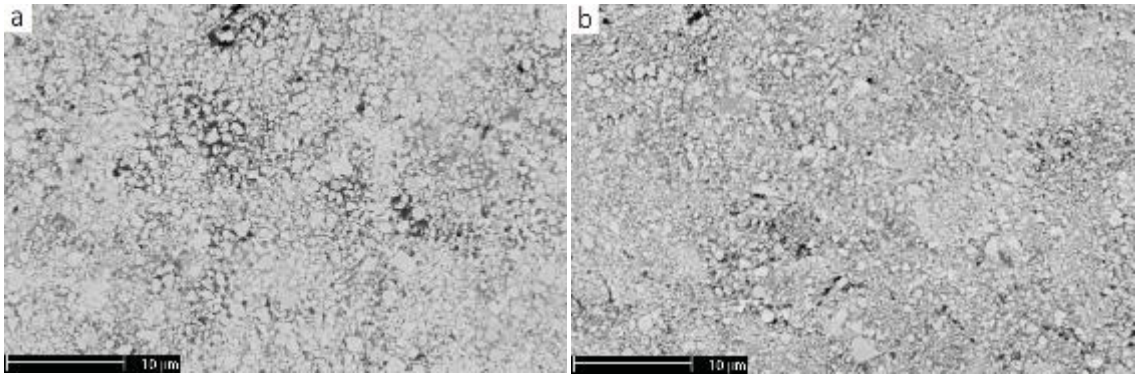

Figure 35. *SEM images of the polished surface microstructure of HVAF sprayed coatings a) W1M3, b) W2M3.*

4.2 Cavitation erosion wear

This section is dedicated to the cavitation erosion results, presenting the samples coated with Cr_3C_2-25NiCr and WC-10Co4Cr in that order. For each material, a graph with the volume loss undergone during the exposure time is analysed and then micrographs for each coating are described.

4.2.1 Cavitation erosion wear of Cr_3C_2-25NiCr coatings

Here, the results for the Cr_3C_2-25NiCr coatings are shown, starting with a volume loss graph and describing then SEM images of gas fuel HVOF, liquid fuel HVOF and HVAF coatings, in that order.

Figure 36 shows the volume loss of Cr_3C_2-25NiCr coatings being exposed to cavitation erosion for 8 hours. Gas fuel HVOF coatings stand as the most worn out with mean erosion rates of 4.03 and 12.02 µm/h for C1DJ and C2DJ, respectively. The best performing coatings were those sprayed with HVAF, having the lowest mean erosion rate of 1.16 µm/h for C1M3. The liquid fuel HVOF sprayed coatings present erosion rates between the mentioned ones but with values closer to those of the HVAF coatings. It has been observed that coatings whose powders were plasma densified have a worse response against cavitation erosion than those that were just agglomerated and sintered. These coatings, as it was observed in section 4.1.1, presented higher levels of carbon dissolution due to finer carbide size that may embrittle the surface, which could explain the lower cavitation erosion resistance.

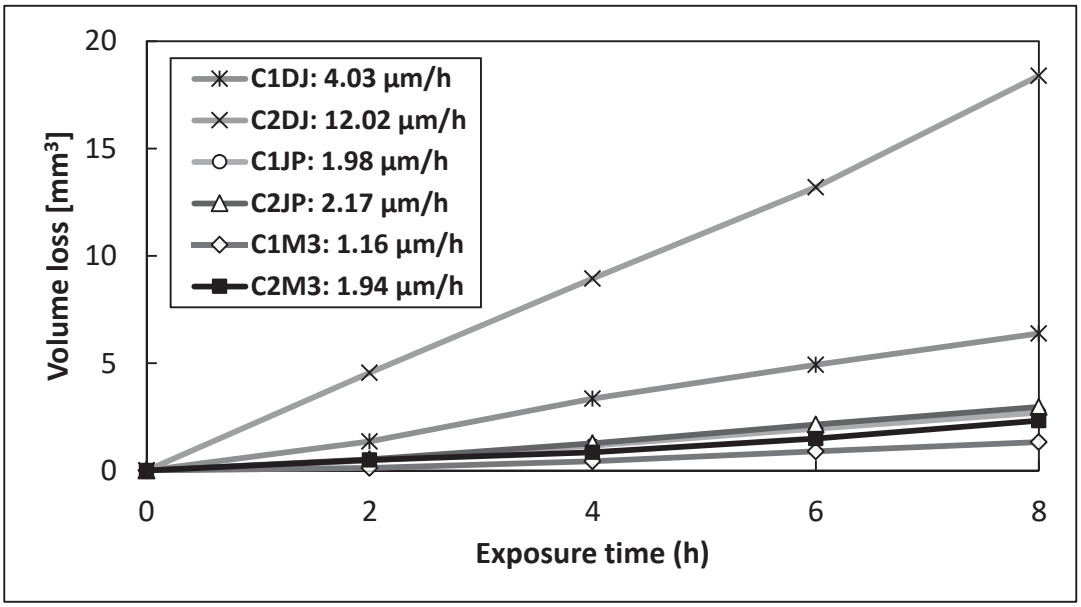

Figure 36. *Cr_3C_2-25NiCr coatings cumulative volume loss and calculated mean erosion rate during cavitation test.*

Matikainen et al. [66] performed cavitation tests to an AISI 316L sample with the same equipment used here, obtaining a mean depth erosion of 2.01 µm/h, a value that is situated between those of the two coatings sprayed with liquid fuel HVOF.

The facts that have been observed in Figure 36 are supported with SEM images of the eroded surfaces in Figure 37-Figure 42. Taking a look at the density of the formed cavities on the wear surface and roughness of the worn surface in the low magnification images,

it can be noticed what it has already been reported: the most eroded surfaces are the gas fuel HVOF coatings and the most resistant ones are those corresponding to the HVAF sprayed coatings. Besides, paying attention to the same features, it can be seen the superior cavitation resistance of those coatings sprayed with agglomerated and sintered powders against the ones sprayed with plasma densified powders.

C1DJ in Figure 37a presents higher surface roughness and bigger cavities than C1JP in Figure 39a. Also, it can be clearly seen in Figure 41a that C1M3 shows the finest wear surface. When looking at the coatings sprayed with plasma densified coatings, the same trend is observed. Surface roughness and cavity frequency are the highest for C2DJ in Figure 37b, features that decrease in C2JP and C2M3 in Figure 39b and Figure 41b respectively.

In the high magnification images cracks (marked in yellow arrows) and flat areas are observed. A lot of the cracks propagate from craters and flat areas. Smooth and flat surfaces are related to material removal by brittle fracture, occurring in weak bonding areas between the splats. Weak interfaces allow cracks to propagate and converge resulting in material loss. These smooth areas are larger for the gas fuel HVOF coatings, especially C2DJ in Figure 38b, and smaller in C1M3 and C2M3 in Figure 42.

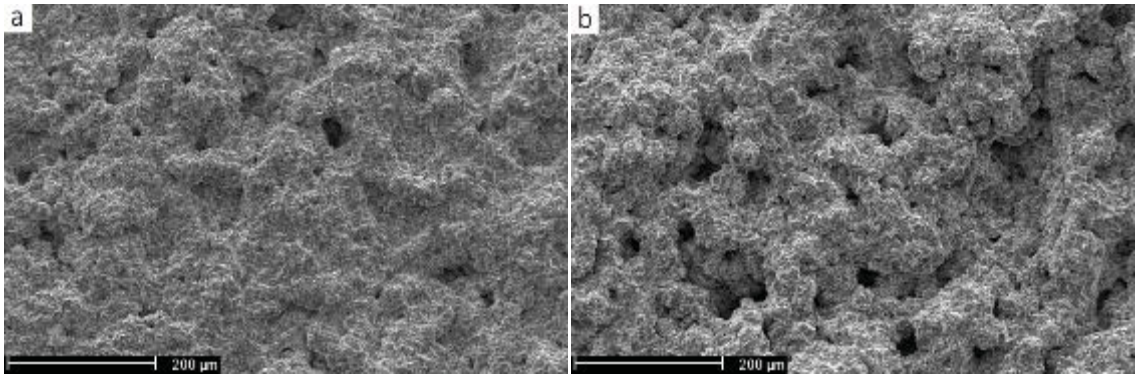

Figure 37. *SEM images of the wear surface topography of HVOF sprayed coatings a) C1DJ, b) C2DJ.*

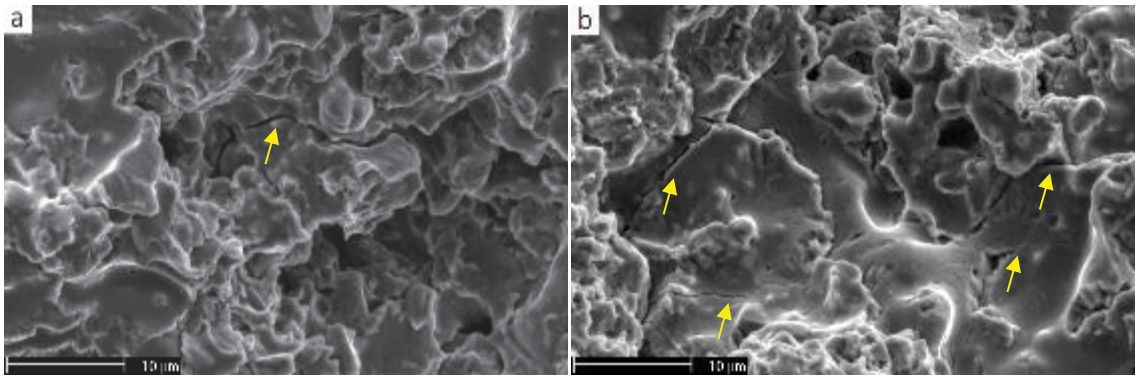

Figure 38. *Detailed SEM images of the wear surface topography of HVOF sprayed coatings a) C1DJ, b) C2DJ.*

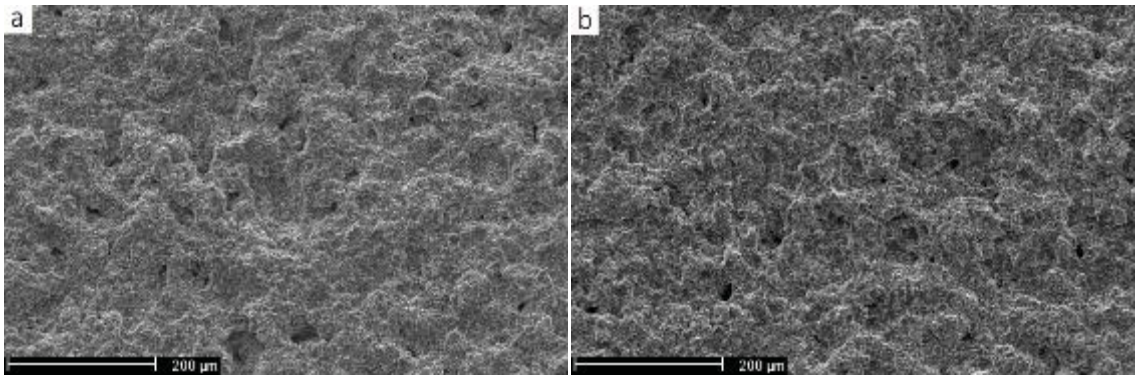

Figure 39. *SEM images of the wear surface topography of HVOF sprayed coatings a) C1JP, b) C2JP.*

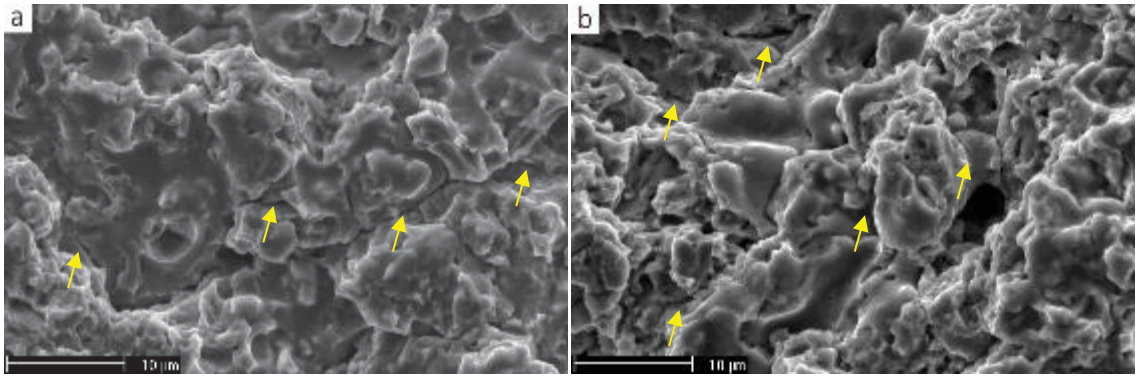

Figure 40. *Detailed SEM images of the wear surface topography of HVOF sprayed coatings a) C1JP, b) C2JP.*

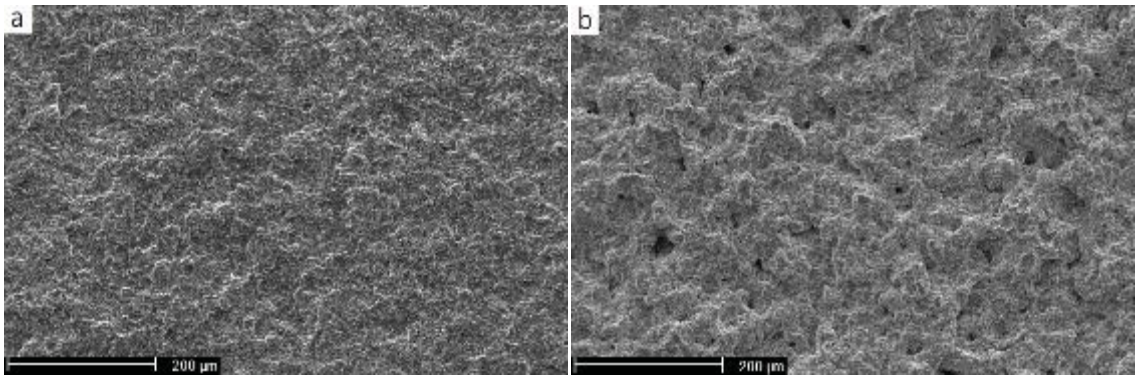

Figure 41. *SEM images of the wear surface topography of HVAF sprayed coatings a) C1M3, b) C2M3.*

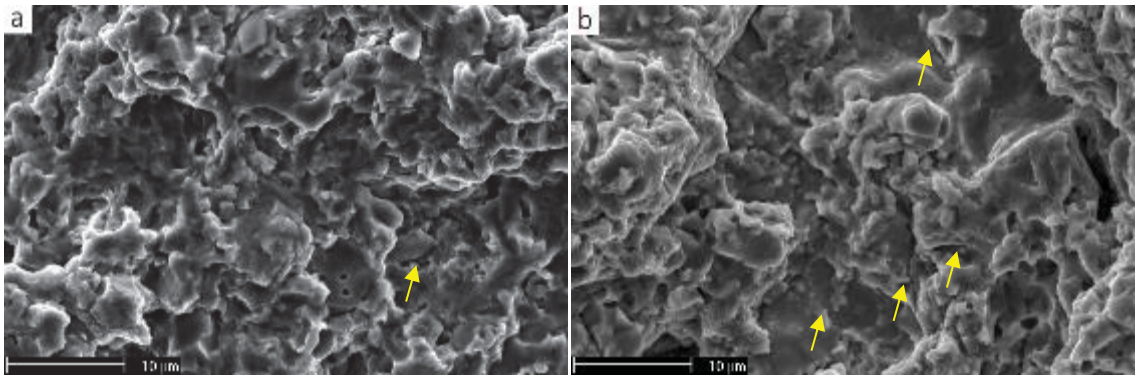

Figure 42. *Detailed SEM images of the wear surface topography of HVAF sprayed coatings a) C1M3, b) C2M3.*

4.2.2 Cavitation erosion wear of WC-10Co4Cr coatings

As done with Cr_3C_2-25NiCr coatings, gas fuel HVOF, liquid fuel HVOF and HVAF samples are described using SEM images after comparing their volume losses during the cavitation test in Figure 43.

The same trend as for Cr_3C_2-25NiCr coatings is observed: gas fuel HVOF coatings appear as the most worn out ones and HVAF coatings present the lowest volume losses. The coatings sprayed with liquid fuel HVOF are situated between the gas fuel HVOF and HVAF coatings. W1DJ has the highest erosion rate with 4.45 µm/h and the lowest mean erosion rate corresponds to W1M3 with 0.35 µm/h. Comparing these results with the mean erosion rate of the AISI 316L sample mentioned in the previous section, which is 2.01 µm/h, gas fuel HVOF coatings are the only ones that exceed its erosion rate.

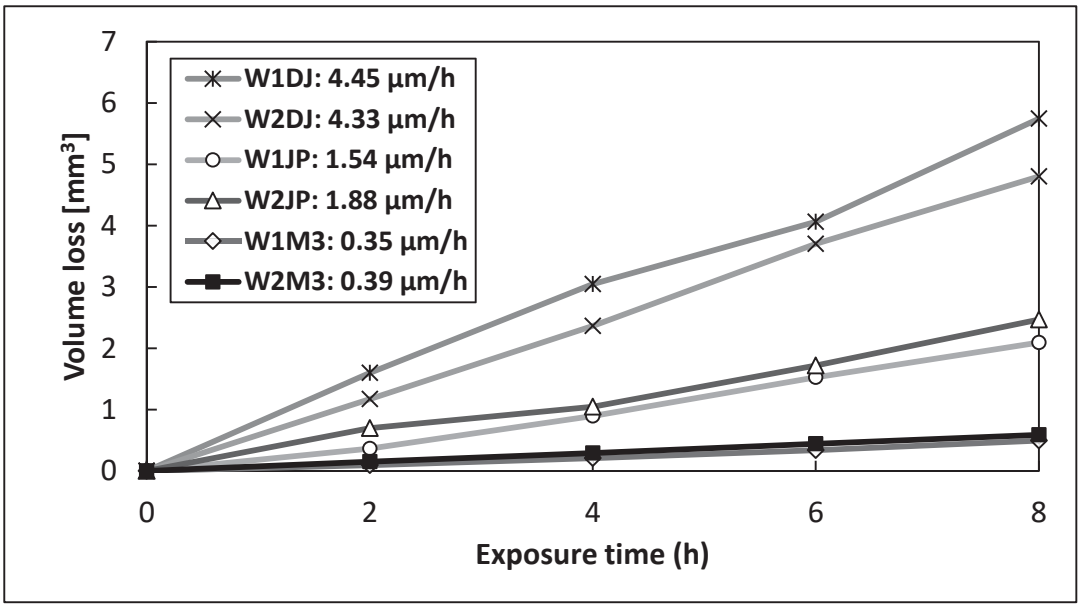

Figure 43. *WC-10Co4Cr coatings volume loss and calculated mean erosion rate during cavitation test.*

Figure 44 to Figure 49 show the coating surfaces after cavitation erosion. All wear surfaces show presence of craters from which cracks (marked in yellow arrows) propagate, as shown in Figure 45a and Figure 47b, but they are more frequent in the HVOF samples. Carbon dissolution is observed as well for W1DJ, W2DJ and W1JP, as it can be noticed in Figure 45a-b and Figure 47b, a feature that could explain the presence of flat areas in their surfaces caused by brittle fracture.

Surface roughness and cavity density are the highest for W1DJ and W2DJ, while W1M3 and W2M3 present the finer wear surface. Polished areas due to low wear rate can still be found in some of the eroded surfaces as shown in the high magnification images of Figure 47a and Figure 49a-b. These polished areas are even visible in the low magnification images of the HVAF coatings in Figure 48, which means that they experienced the lowest volume loss as reported in Figure 43.

In Figure 45, detailed images of gas fuel HVOF coatings present a blocky structure with flat areas as a result of brittle wear. The wear mechanism seems to be the removal of splats as a result of crack propagation from weak boundaries due to poor intersplat bonding. In liquid fuel HVOF and HVAF coatings, material removal occurred by the pull out of smaller particles leaving a wear surface without the sharp edges found in W1DJ and W2DJ. W2JP in Figure 47b seems to have both wear mechanisms since it can be seen the roughness left by the pull out of small particles and a cavity originated from a splat removal. In Figure 49, where there are still polished areas in the HVAF coatings, it is noticeable how material removal starts in the polished surface as small pits from which

cracks propagate and converge leading to bigger cavities. The two types of wear mechanisms observed can be caused by the amount of carbon diluted into the metal matrix, presenting brittle wear those coatings with the highest levels of dissolution, i.e. W1DJ, W2DJ and W2JP, and ductile wear W1JP and the HVAF coatings with lower carbon dissolution.

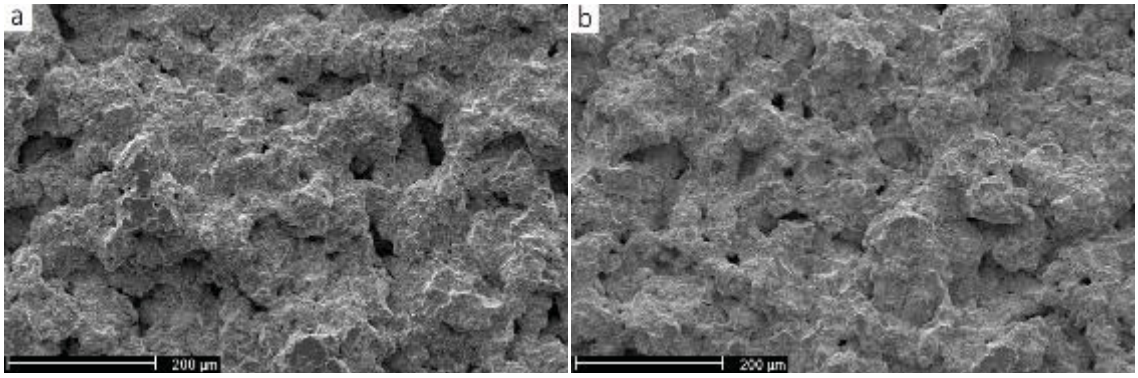

Figure 44. *SEM images of the wear surface topography of HVOF sprayed coatings a) W1DJ, b) W2DJ.*

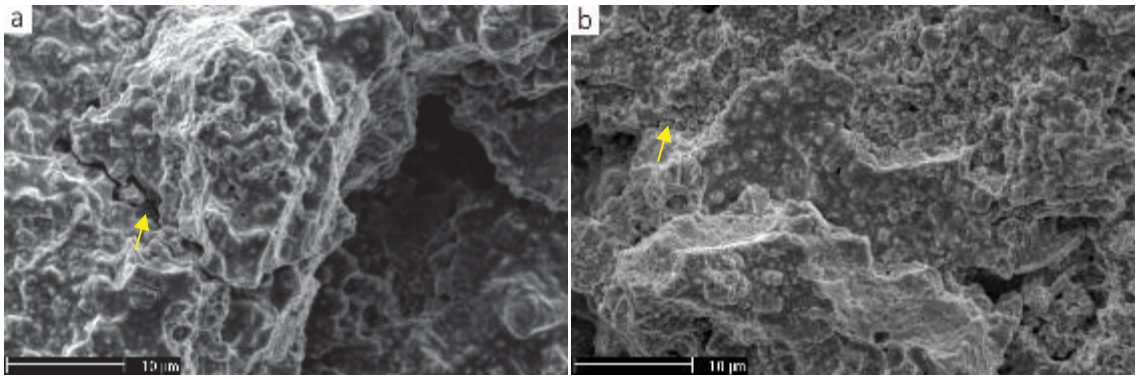

Figure 45. *Detailed SEM images of the wear surface topography of HVOF sprayed coatings a) W1DJ, b) W2DJ.*

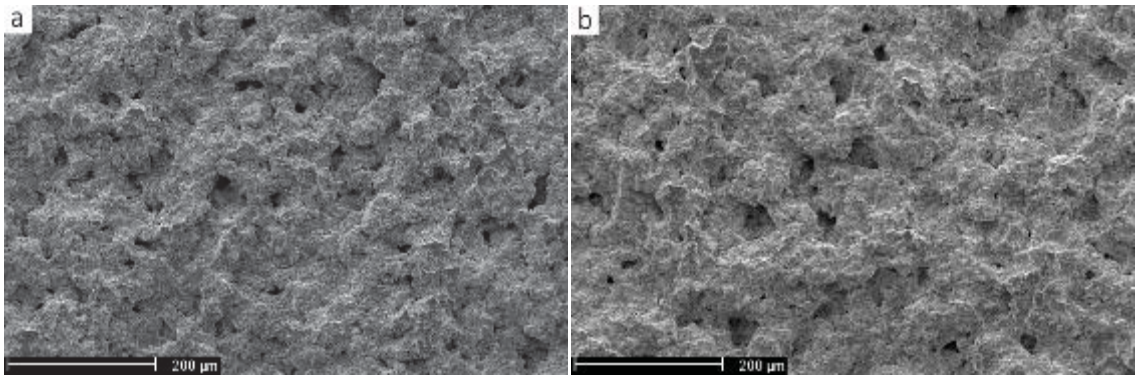

Figure 46. *SEM images of the wear surface topography of HVOF sprayed coatings a) W1JP, b) W2JP.*

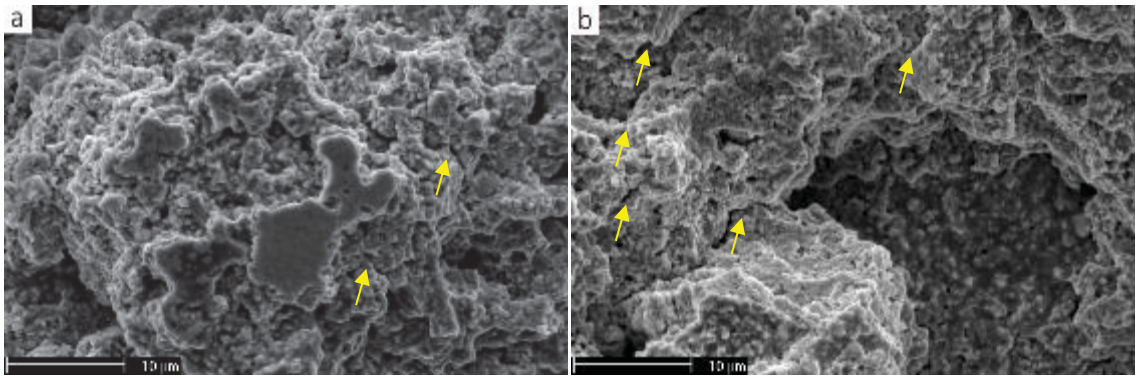

Figure 47. *Detailed SEM images of the wear surface topography of HVOF sprayed coatings a) W1JP, b) W2JP.*

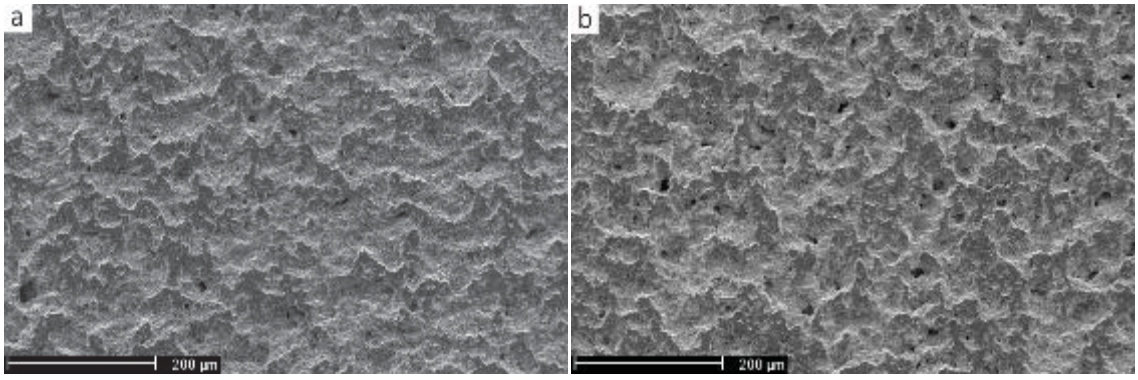

Figure 48. *SEM images of the wear surface topography of HVAF sprayed coatings a) W1M3, b) W2M3.*

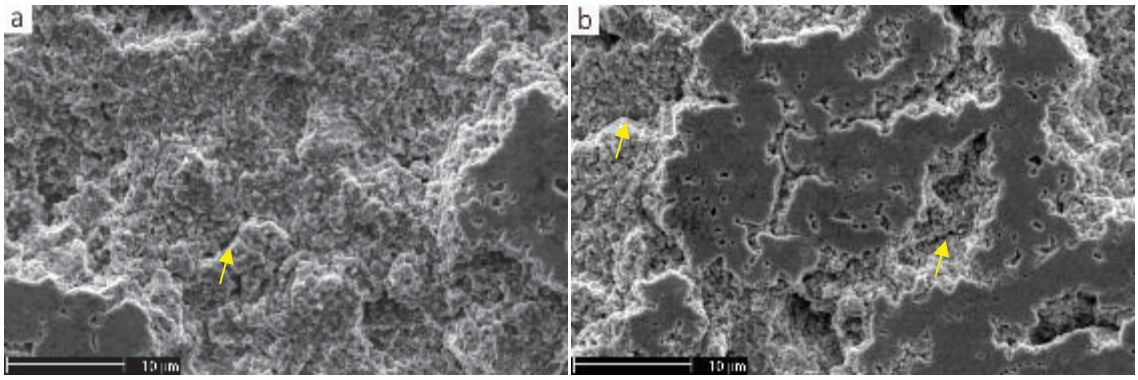

Figure 49. *Detailed SEM images of the wear surface topography of HVAF sprayed coatings a) W1M3, b) W2M3.*

4.3 Slurry erosion wear

Apart from doing slurry erosion tests with hardmetal coatings, a reference sample was tested as well to compare the results between bulk steel and coatings, as well as the effect of the erodent size. The reference samples are uncoated AISI 316L stainless steel, whose volume losses are shown in Figure 50.

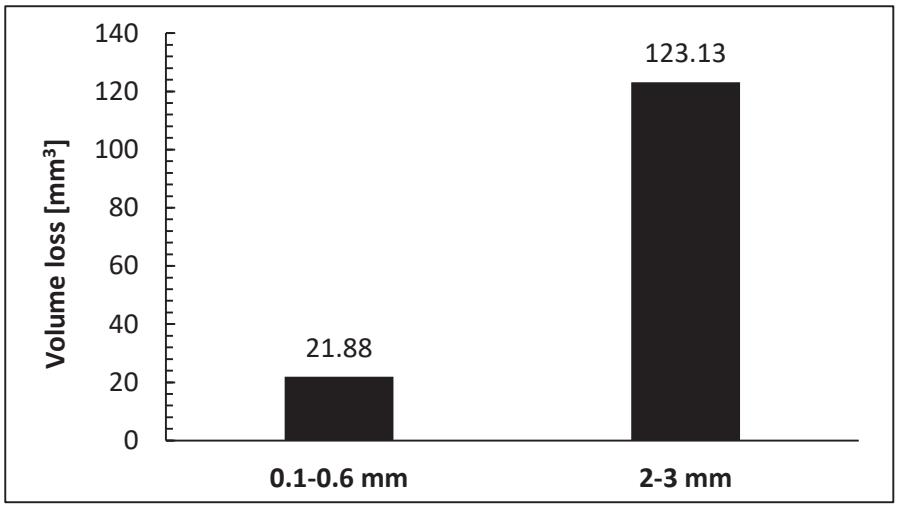

Figure 50. *Volume loss of AISI 316L stainless steel sample tested with 0.1-0.6 mm and 2-3 mm quartz size particles.*

The volume loss produced with the 2-3 mm quartz size particles is almost 6 times bigger than that with the 0.1-0.6 mm particles. This demonstrates that an increase in the erodent particle size causes an increase in the volume loss since the impact energy is significantly higher, a fact that will remain for the coatings results.

Figure 51 shows the eroded surfaces of AISI 316L stainless steel. It is noticeable that the wear marks caused by the coarse erodent particles have the same features as the fine particles but they are much more pronounced and deformed. Cutting and ploughing marks

are visible on both surfaces and loosened platelets are observed on the sample tested with coarse particles, especially in the high magnification image shown in Figure 51b. Wear marks are pointed out in the images with red arrows for cutting, yellow ellipses for ploughing and red squares for loosened platelets.

The following sections are dedicated to Cr_3C_2-25NiCr and WC-10Co4Cr results.

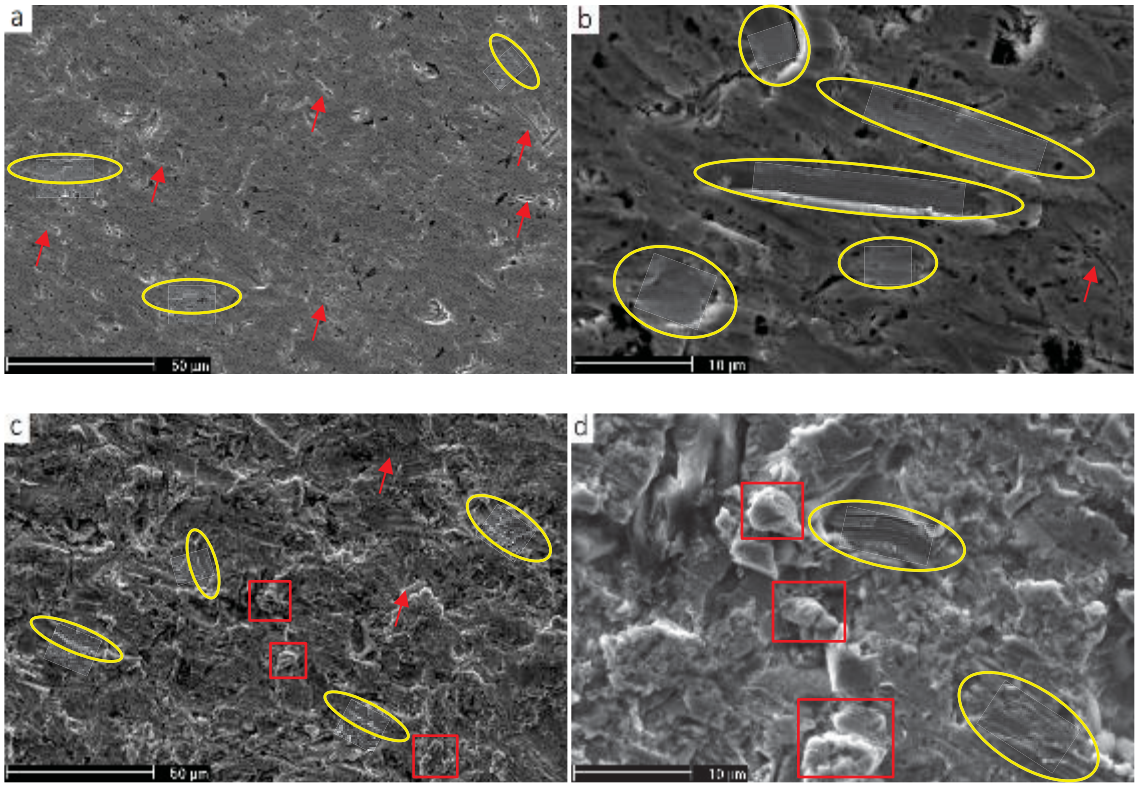

Figure 51. *SEM images of the wear surface topography of AISI 316L stainless steel. a), b) tested with 0.1-0.6 mm quartz particles and c), d) with 2-3 mm quartz particles.*

4.3.1 Slurry erosion wear of Cr_3C_2-25NiCr coatings

There were six different coatings of Cr_3C_2-25NiCr and they were tested with two different quartz sizes. Both test results are presented in Figure 52 simultaneously and then micrographs will serve to describe the coatings wear surfaces.

Starting with the 0.1-0.6 mm quartz size test results, the average volume loss of the tested Cr_3C_2-25NiCr coatings is 0.84 mm^3. Here, the gas fuel HVOF coatings and the HVAF coating C1M3 have high volume loss values, highest for C1DJ with 1.23 mm^3. Liquid fuel HVOF coatings have medium values while the HVAF coating C2M3 has the smallest one with 0.38 mm^3. Next, the 2-3 mm quartz size test results have an average volume loss of 25.49 mm^3. In this case HVAF coatings experienced the largest and smallest volume

losses for C1M3 and C2M3 coatings with values of 42.26 mm^3 and 14.51 mm^3 respectively. The second most worn coating was C1DJ with 30.97 mm^3 and the rest of the coatings present volume losses below the average.

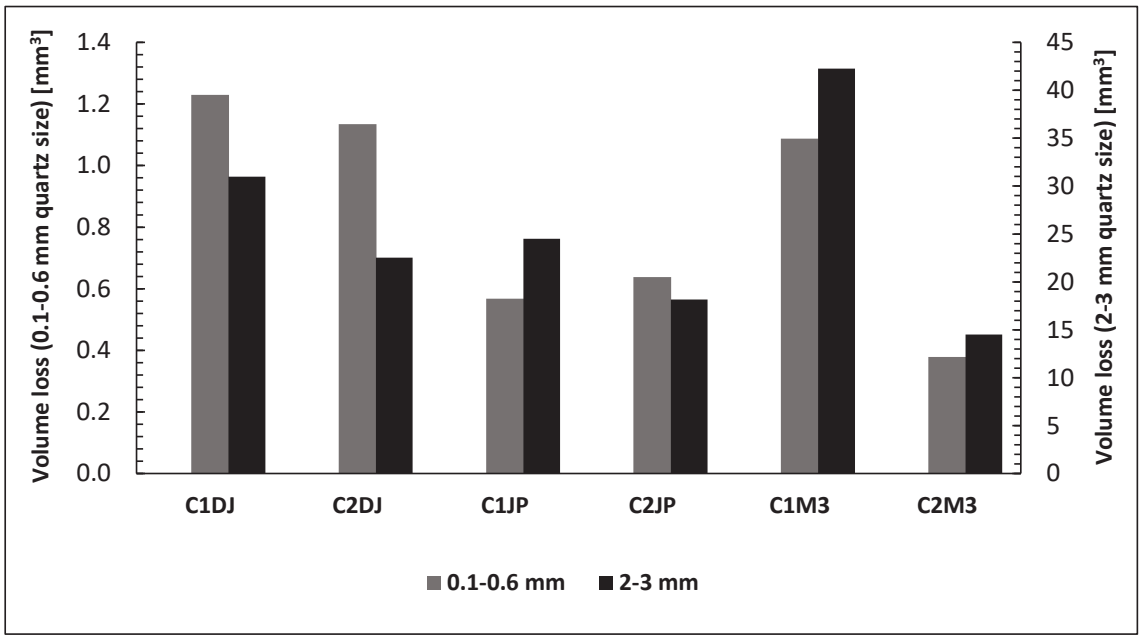

Figure 52. *Cr_3C_2-25NiCr coatings volume loss (mm^3) during slurry pot test.*

Once the volume loss for each coating is known, the wear surface topography is described in the following. Micrographs of coatings tested with the two quartz sizes are shown simultaneously and these are compared with the other coating sprayed with the same technique.

Figure 53 and Figure 54 show the macro- and micro-surface morphology for the propane fuelled HVOF coatings after the slurry erosion testing. When the coated samples eroded with fine quartz particles are compared, it can be observed that the C1DJ coating in Figure 53a shows uniform wear along the surface, whereas C2DJ presents locations smoother than others, highlighted with yellow rectangles in the image. The smooth areas do not have as many pits, which are pointed out with blue arrows, as C1DJ. These observations could explain the lower volume loss of the C2DJ coating. The pits observed in both coatings are formed when carbides are pulled out after the removal of the surrounding metal matrix.

In Figure 54a and b, detailed SEM images allow a closer analysis of C1DJ and C2DJ surfaces. Cutting and resulting removal of material by the quartz particles is noticeable on the surface of C1DJ. Some marks of ploughing and cracking of the carbides are pointed out with yellow ellipses and yellow arrows respectively. Similar removal of material and cutting of the surface are also visible on C2DJ, but to a lesser extent. What seems to be preventing the uniform surface wear on C2DJ coating are the areas with finer carbide size

present in Figure 54b and marked with blue ellipses. These areas result from complete melting of the powder particle in plasma densification process and they seem to provide a higher hardness than the rest of the coating, being more resistant to the grits abrasion. However, defects on the polished surface of C2DJ were found to result in decreased abrasion resistance. These defects that could have occurred during the grinding and polishing process are pits and cracks propagated from weak particle boundaries.

In Figure 53c and d, the samples eroded with coarse particles do not show pits anymore, since these have coalesced in larger eroded areas all over the coating leaving an irregular surface where the soft binder is removed first, thus occupying a deeper level than the carbides. C2DJ presents again some areas smoother than others more resistant to abrasion, highlighted by yellow rectangles.

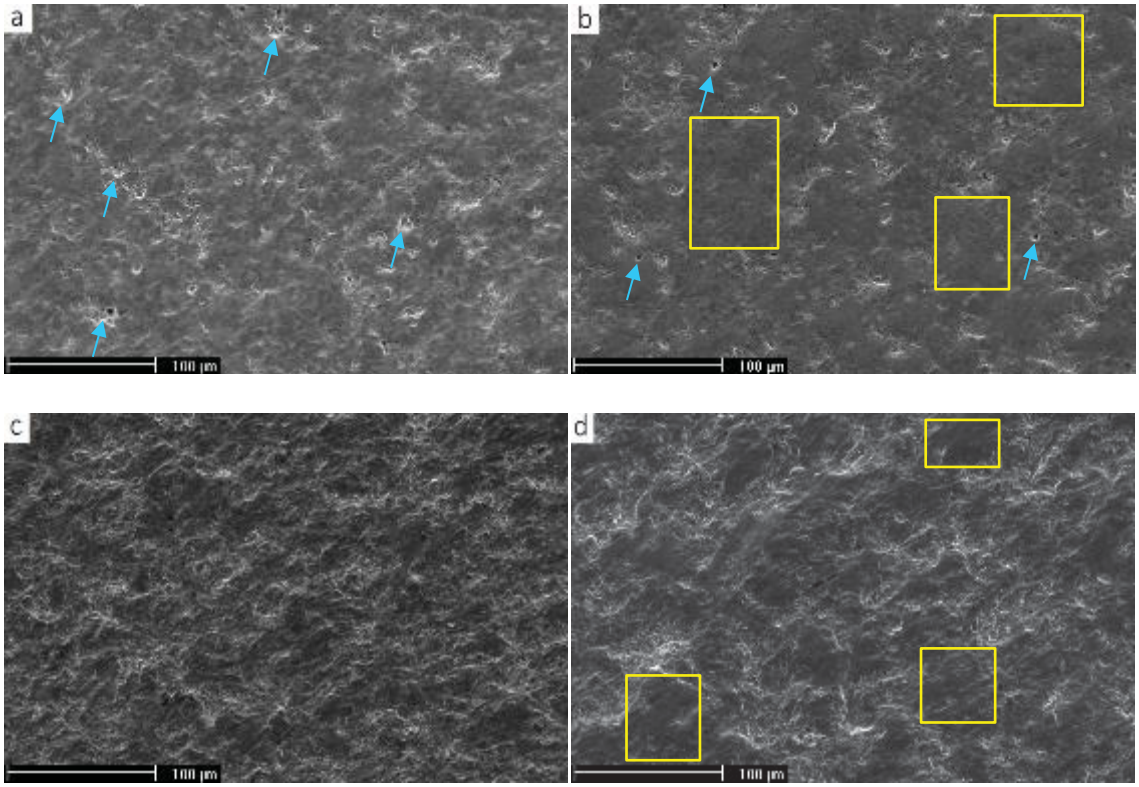

Figure 53. *SEM images of the wear surface topography of HVOF sprayed coatings a) C1DJ tested with 0.1-0.6 mm quartz size, b) C2DJ tested with 0.1-0.6 mm quartz size, c) C1DJ tested with 2-3 mm quartz size, d) C2DJ tested with 2-3 mm quartz size.*

Looking at the high magnification images, Figure 54c highlights ploughing and plastic deformation, yellow ellipses and green rectangles respectively, caused by the erodent flow on the surface of C1DJ. Shallower scratches and multiple cracks in a carbide marked in yellow arrows are also visible. In Figure 54d the direction of abrasion with cutting marks, represented with red arrows, can be noticed also for C2DJ coating. In this case,

material is being removed around splats that will be finally pulled out, which leaves some areas more worn out than others resulting in the observed topography of C2DJ.

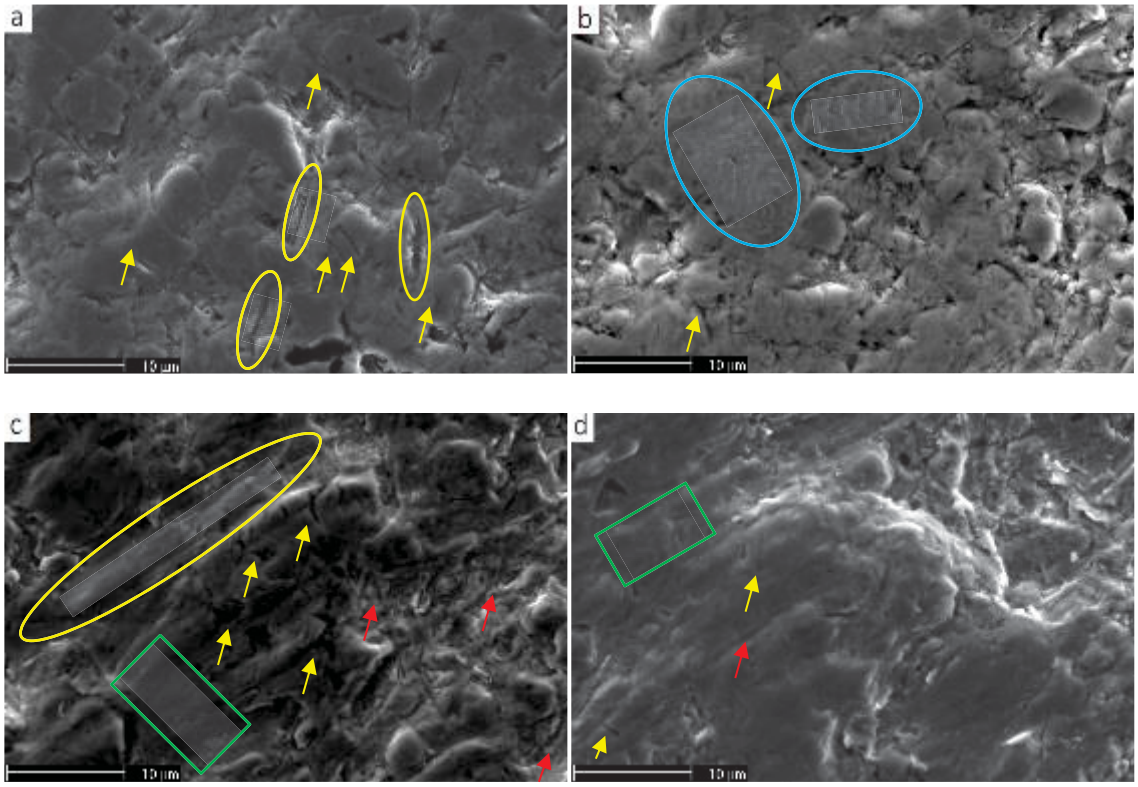

Figure 54. *Detailed SEM images of the wear surface topography of HVOF sprayed coatings a) C1DJ tested with 0.1-0.6 mm quartz size, b) C2DJ tested with 0.1-0.6 mm quartz size, c) C1DJ tested with 2-3 mm quartz size, d) C2DJ tested with 2-3 mm quartz size.*

The eroded liquid fuel HVOF sprayed coatings are shown in Figure 55 and Figure 56. For the fine quartz size test, in Figure 55a and b, it is noticed that C1JP has a uniformly worn out and rougher surface than C2JP whose topography is generally smoother with some weak spots of craters, marked with blue arrows, identical to that of C1DJ and C2DJ. Fractures in the carbide particles of C1JP are visible in the detailed SEM image presented in Figure 56a, highlighted by yellow arrows. The removal of the metal matrix can be seen as well as the path left by quartz while cutting its surface, marked in red arrows. On the other hand, a crater can be seen on the surface of C2JP surrounded by areas with finer carbides, marked with blue ellipses, in Figure 56b. This crater could have been formed due to a zone with poor adhesion between splats. Cracks in the carbides are also present, marked as yellow arrows.

The samples eroded with the coarse particles present higher levels of wear as shown in Figure 55c and d. For the high magnification images of C1JP surface, in Figure 56c, the rounded carbides are clearly sticking out of the coating. The more aggressive erosion of the metal matrix, which is therefore removed first, has left the carbides on a higher level

compared to the metal matrix. Cutting marks and fractures in carbide particles are highlighted by red and yellow arrows, respectively. On the other hand, in Figure 56d corresponding to C2JP, a splat is located in the centre with a higher abrasion resistance than its surroundings since it has less material removal. However, this area contains cracks and plastic deformation marked in the image by the yellow arrows and green rectangles, respectively.

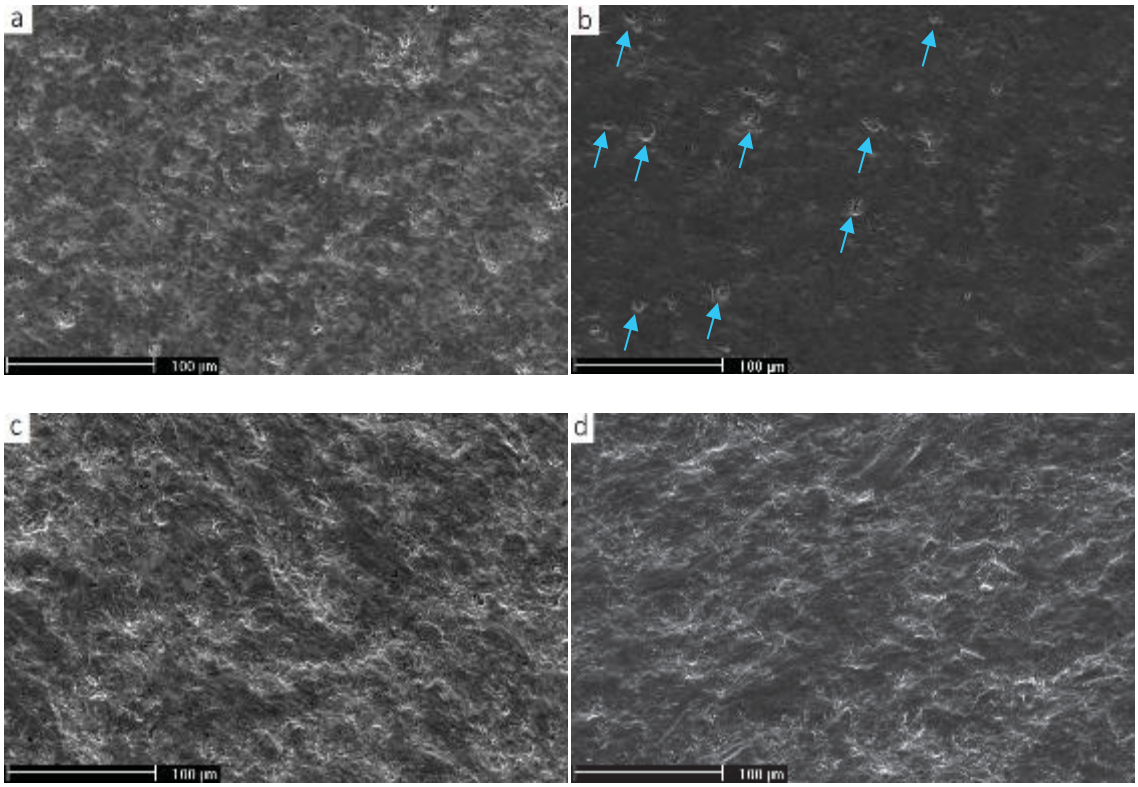

Figure 55. *SEM images of the wear surface topography of HVOF sprayed coatings a) C1JP tested with 0.1-0.6 mm quartz size, b) C2JP tested with 0.1-0.6 mm quartz size, c) C1JP tested with 2-3 mm quartz size, d) C2JP tested with 2-3 mm quartz size.*

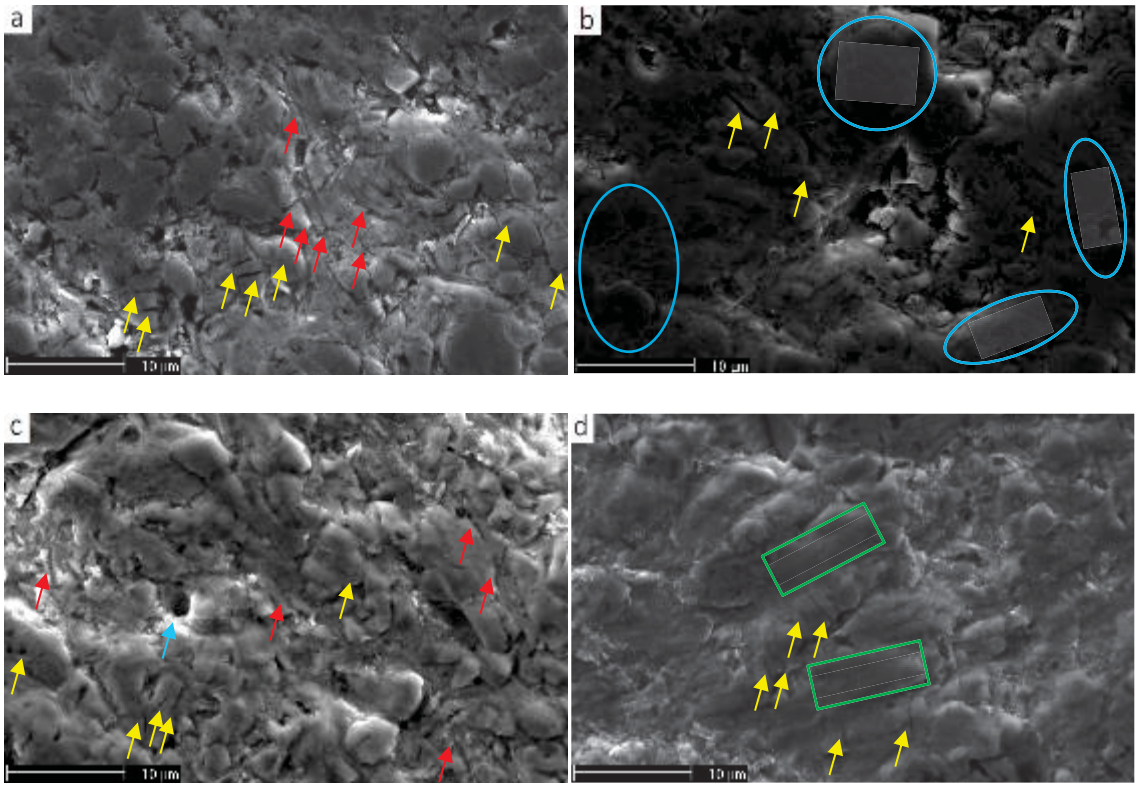

Figure 56. *Detailed SEM images of the wear surface topography of HVOF sprayed coatings a) C1JP tested with 0.1-0.6 mm quartz size, b) C2JP tested with 0.1-0.6 mm quartz size, c) C1JP tested with 2-3 mm quartz size, d) C2JP tested with 2-3 mm quartz size.*

Finally, Figure 57 and Figure 58 present the wear surface topography of HVAF coatings C1M3 and C2M3. Starting with the samples tested with fine quartz in Figure 57a and b, C1M3 is clearly much more eroded than C2M3 which only presents pits, marked as blue arrows, having the rest of the surface showing a smooth appearance. Two distinctive levels of deepness can be observed on the worn surface of C1M3. The deeper worn areas correspond to the soft matrix and the higher areas to the harder carbides. Looking at the detailed surface morphology in Figure 58a, the surface shows a detail of a void left by a carbide that has been pulled out. Here, the direction of abrasion is noticeable as well as the cutting marks, highlighted by red arrows. In Figure 58b there are some grooves outlining the carbides and areas of finer carbides, marked as blue ellipses, in C2M3.

Figure 57c-d and Figure 58c-d are from the surfaces that were eroded with coarse quartz. In the low magnification images, the surface topographies are similar for both coatings. However, the cutting marks, marked in red arrows, seem deeper on C1M3 and show the flow direction of quartz particles. Figure 58c shows a detailed area with removal of soft binder by the erodent flow impacting with a low angle. The cutting marks show the path followed by the erodent and contain some quartz particles embedded on the coating after

colliding with a carbide. The same feature is shown for C2M3 in Figure 58d. Some cracks are marked with yellow arrows as well as the quartz particle with a blue square.

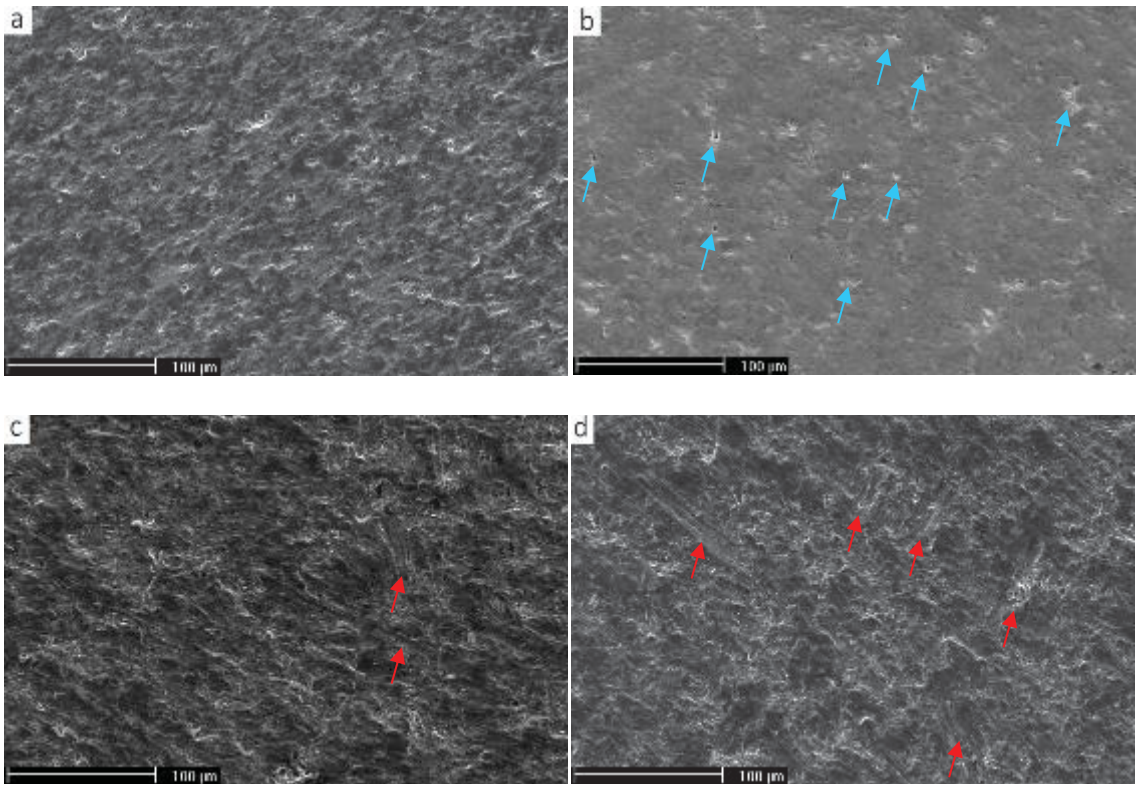

Figure 57. *SEM images of the wear surface topography of HVAF sprayed coatings a) C1M3 tested with 0.1-0.6 mm quartz size, b) C2M3 tested with 0.1-0.6 mm quartz size, c) C1M3 tested with 2-3 mm quartz size, d) C2M3 tested with 2-3 mm quartz size.*

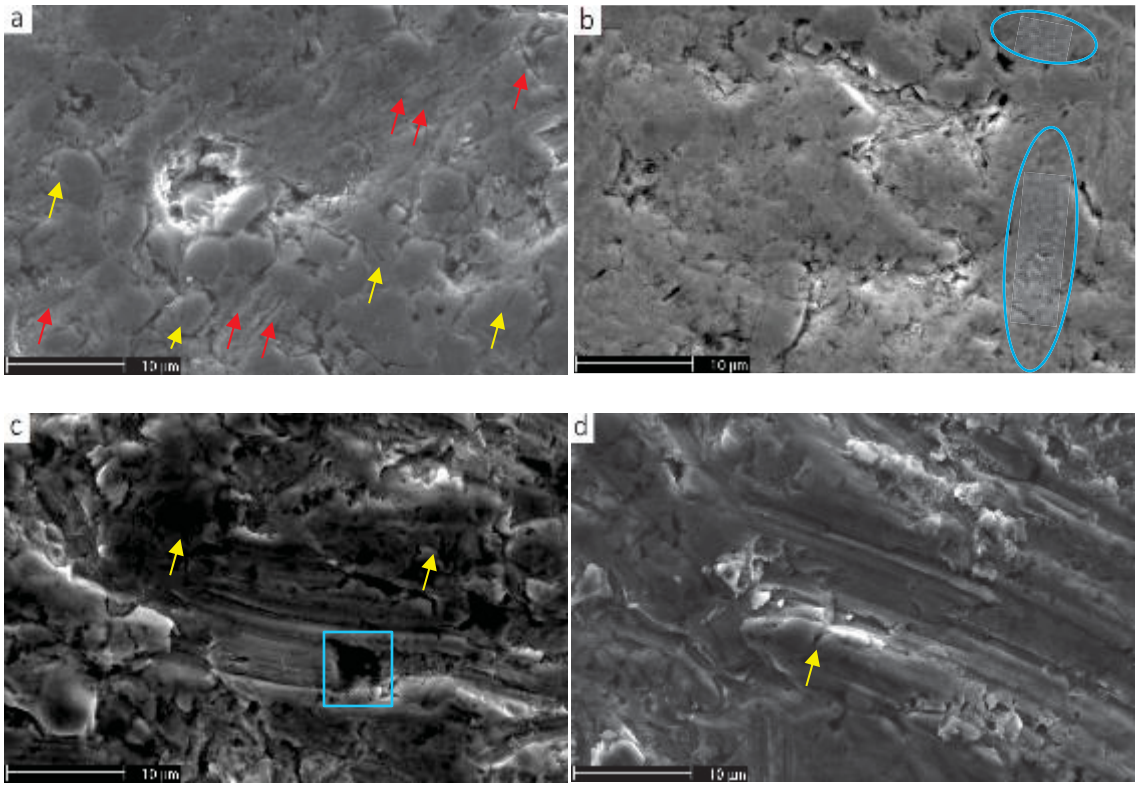

Figure 58. *Detailed SEM images of the wear surface topography of HVAF sprayed coatings tested a) C1M3 tested with 0.1-0.6 mm quartz size, b) C2M3 tested with 0.1-0.6 mm quartz size, c) C1M3 tested with 2-3 mm quartz size, d) C2M3 tested with 2-3 mm quartz size.*

4.3.2 Slurry erosion wear of WC-10Co4Cr coatings

The slurry erosion results of the WC-10Co4Cr coatings are presented in Figure 59. Afterwards, detailed micrographs of the eroded surfaces are described similar to Cr_3C_2-25NiCr coatings in the previous section.

The test results with a quartz size between 0.1 and 0.6 mm have an average volume loss of the tested WC-10Co4Cr coatings of 0.13 mm^3. It can be noticed that the smallest volume loss values were determined for the HVAF and liquid fuel HVOF sprayed coatings, ranging from 0.01 mm^3 for W2M3 to 0.07 mm^3 for W1M3 and W2JP. Here, the average volume loss of liquid fuel HVOF sprayed coatings is bigger than the one for HVAF coatings. The gas fuel HVOF sprayed coatings appeared to wear the most with 0.33 mm^3 volume loss for W1DJ. On the other hand, the average weight loss for the 2-3 mm quartz size test results was 5.04 mm^3. The HVAF coatings appear as the least worn out ones as the lowest volume loss was measured for the W1M3 with 3.94 mm^3. Liquid fuel HVOF sprayed coatings presented the highest wear rates with 5.93 mm^3 for W2JP while rest of the coatings stand between the mentioned ones.

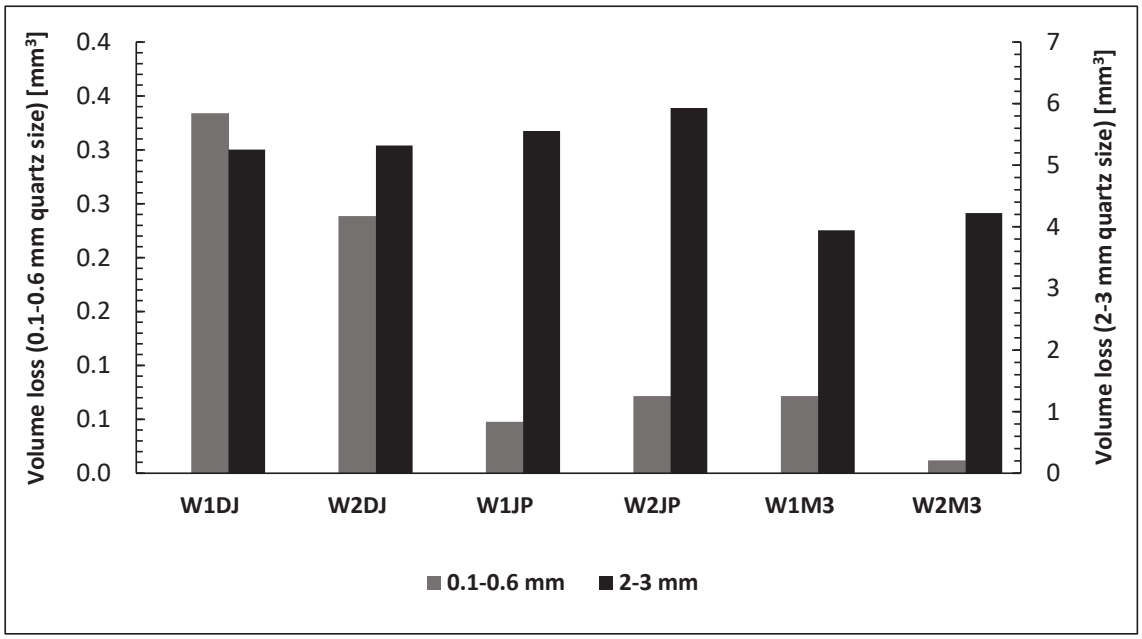

Figure 59. *WC-10Co4Cr coatings volume loss (mm^3) during slurry pot test.*

WC-10Co4Cr coatings experienced less volume loss than the samples coated with Cr_3C_2-25NiCr. The average volume loss of WC-10Co4Cr coatings was 5 times lower than that of the Cr_3C_2-25NiCr coatings when 2-3 mm quartz size test is considered. Comparing the results with the average volume loss of the stainless steel samples, WC-10Co4Cr coatings average volume losses were approximately 168 and 25 times smaller than the ones for the stainless steel reference sample in the tests carried out with 0.1-0.6 and 2-3 mm quartz sizes, respectively. Similarly, both coatings and the reference sample experience higher volume loss with the larger erodent particle size. After analysing the column graph, micrographs for each coating are presented next.

Figure 60 and Figure 61 are the surfaces of the gas fuel HVOF sprayed coatings after the slurry erosion test. As shown in Figure 60a and b, the surfaces tested with 0.1-0.6 mm erodent have a similar topography with pits, marked in blue arrows, formed when carbides are pulled out and metal matrix is exposed to the quartz impacts. The metallic matrix is easily removed due to the lower hardness. W2DJ has a bigger concentration of these wear marks than W1DJ. Figure 61a and b show the formed pits in higher magnification. It can be noticed that some coating particles, marked with yellow squares, have become loosened and could soon be chipped off on the surface of W1DJ. Crack formation can be observed in the formed pit, marked in yellow arrow, a phenomenon already reported by Thakur et al. [52]. In W2DJ, Figure 61b, some smooth regions of metallic matrix are visible, marked with blue ellipses.

Looking at the samples eroded with 2-3 mm quartz particles, in Figure 60c and d plastic deformation is observed in the form of grooves, highlighted by yellow ellipses, which are more frequent in W2DJ. Similar features have already been observed by Wang et al. [57]. On the surface of the W1DJ, the black spots marked with red squares are embedded quartz particles fragments. Figure 61c and d present detailed views of the grooves that show also the direction of abrasion. The surfaces also clearly show the bigger carbide size of the feedstock powder used to spray W1DJ coating. Besides, W1DJ presents an area of metallic matrix marked with blue ellipse in Figure 61c.

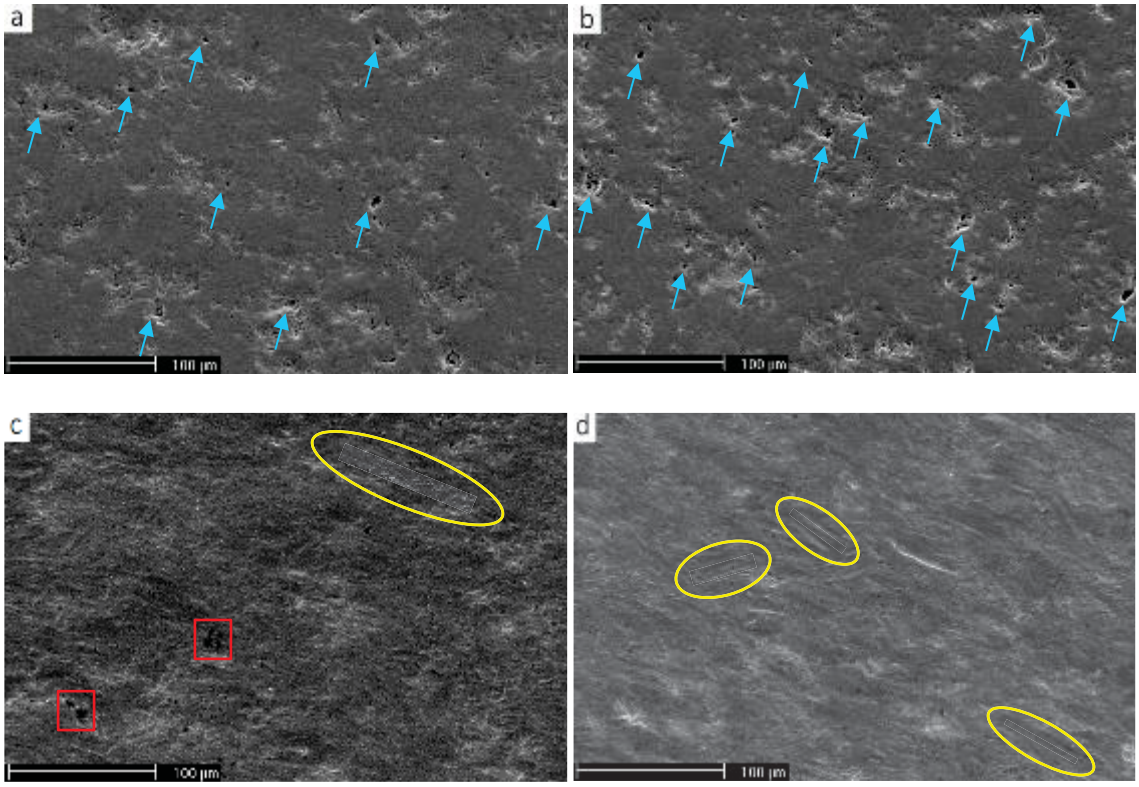

Figure 60. *SEM images of the wear surface topography of HVOF sprayed coatings a) W1DJ tested with 0.1-0.6 mm quartz size, b) W2DJ tested with 0.1-0.6 mm quartz size, c) W1DJ tested with 2-3 mm quartz size, d) W2DJ tested with 2-3 mm quartz size.*

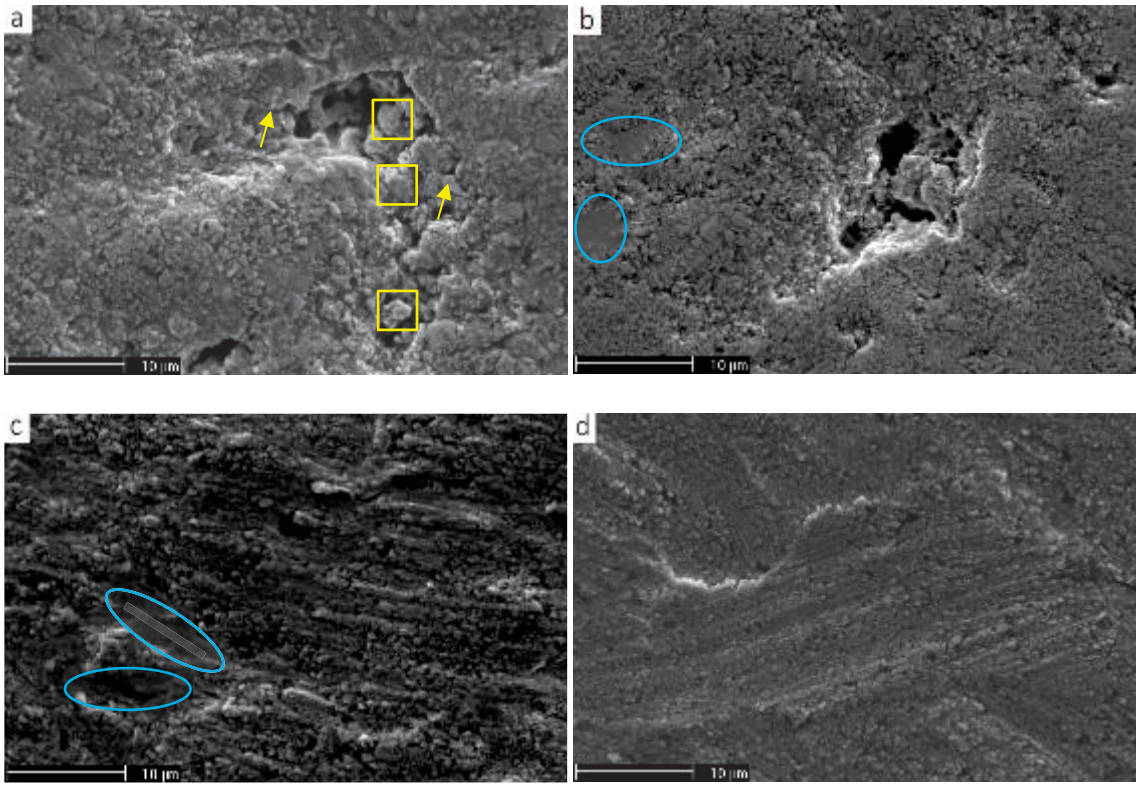

Figure 61. *Detailed SEM images of the wear surface topography of HVOF sprayed coatings a) W1DJ tested with 0.1-0.6 mm quartz size, b) W2DJ tested with 0.1-0.6 mm quartz size, c) W1DJ tested with 2-3 mm quartz size, d) W2DJ tested with 2-3 mm quartz size.*

Figure 62 and Figure 63 show eroded surfaces of the coatings sprayed with kerosene fuelled HVOF. Pits, marked in blue arrows, are observable for the coatings tested with fine erodent particles in Figure 62a and b similar to the gas fuel HVOF sprayed coatings. W2JP presents higher concentration of wear marks. In Figure 63a and b the carbide pull-outs and eruption of metal matrix can be seen closer. Both images present pits and loosened carbides highlighted by red squares.

In the macro-surface morphologies for the coatings eroded with coarse particles, Figure 62c and d, plastic deformation and grooves can be seen in yellow ellipses. Figure 63c and d show details of grooves for both coatings and loosened carbides marked with red squares in C2JP.

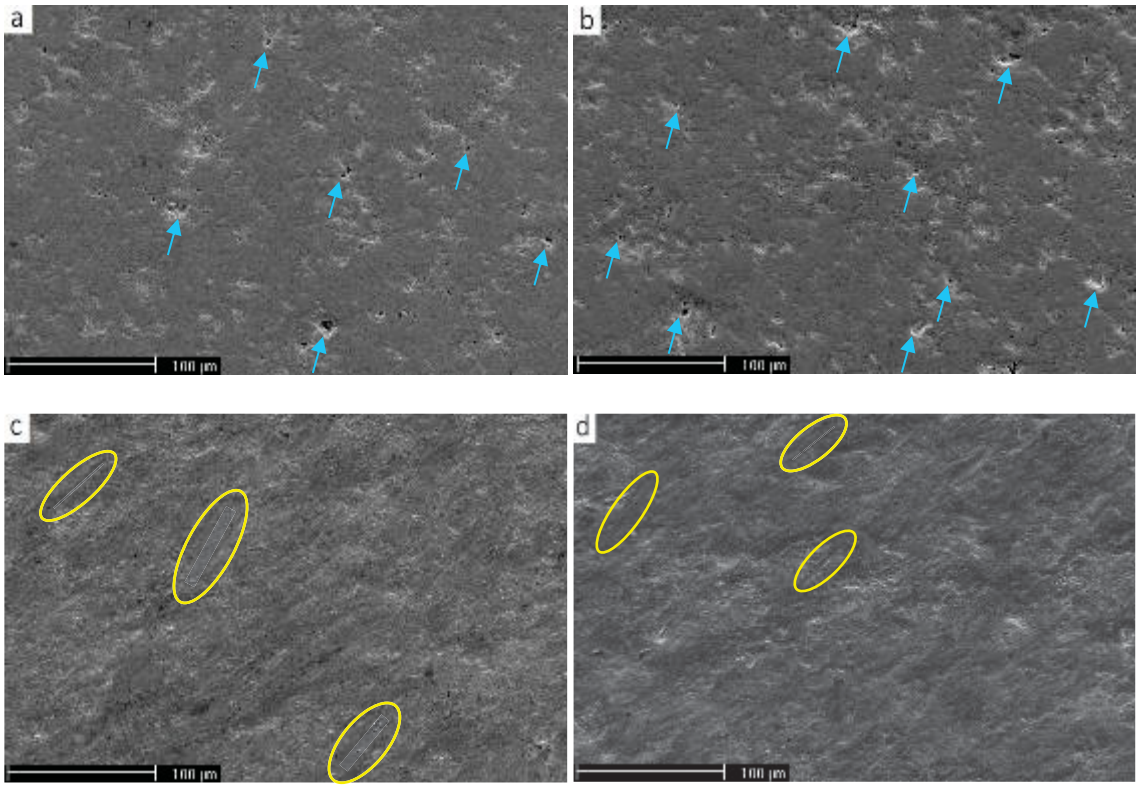

Figure 62. *SEM images of the wear surface topography of HVOF sprayed coatings a) W1JP tested with 0.1-0.6 mm quartz size, b) W2JP tested with 0.1-0.6 mm quartz size, c) W1JP tested with 2-3 mm quartz size and d) W2JP tested with 2-3 mm quartz size.*

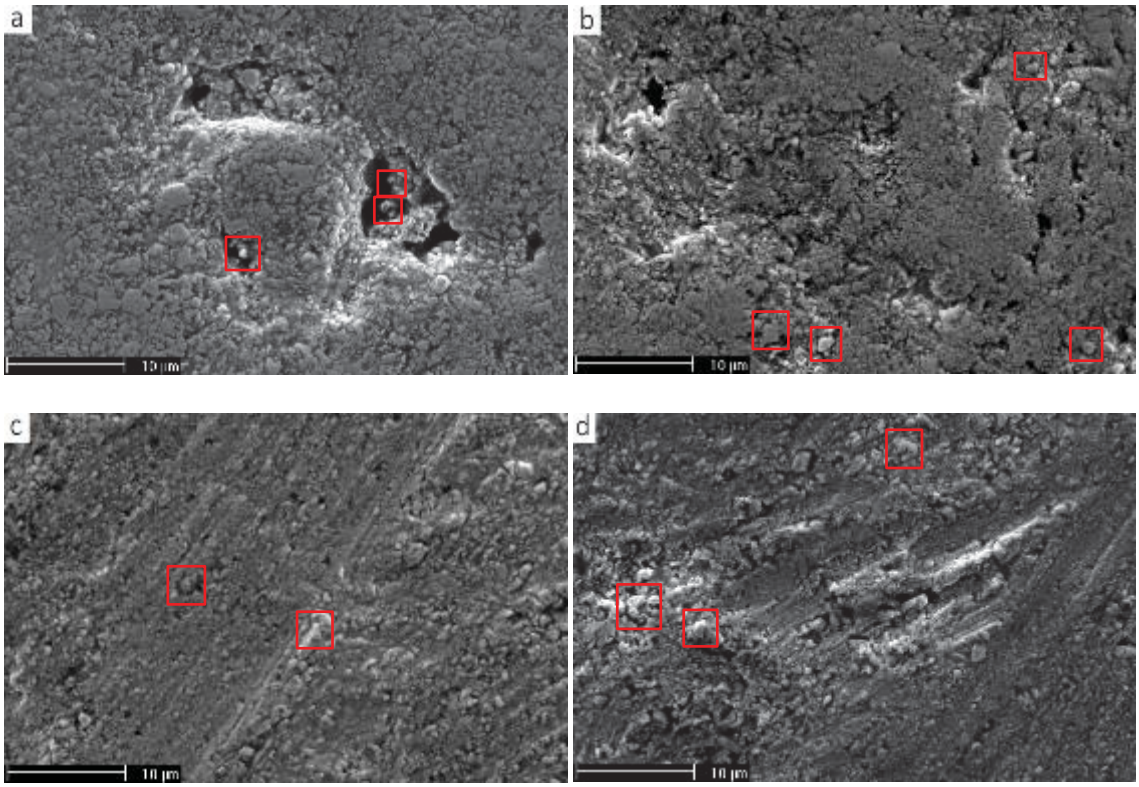

Figure 63. *Detailed SEM images of the wear surface topography of HVOF sprayed coatings a) W1JP tested with 0.1-0.6 mm quartz size, b) W2JP tested with 0.1-0.6 mm quartz size, c) W1JP tested with 2-3 mm quartz size, d) W2JP tested with 2-3 mm quartz size.*

Finally, HVAF coatings are shown in Figure 64 and Figure 65. In Figure 64a and b the coatings tested with 0.1-0.6 mm quartz size present wear marks, marked in blue arrows, caused by carbides being pulled out and matrix removed after being exposed to the impacting erodent particles. Taking a look to the detailed images, in Figure 65a and b, the W1M3 coating surface shows a location with large cluster of metallic matrix and in W2M3 there are areas where the soft binder has been removed leaving loosened carbides highlighted by red squares.

The surfaces left by the slurry erosion with coarse particles have a similar topography characterised by plastic deformation seen in the grooves marked with yellow ellipses as shown in Figure 64c and d. The detailed images in Figure 65c and d show these wear marks and loosened carbides as well.

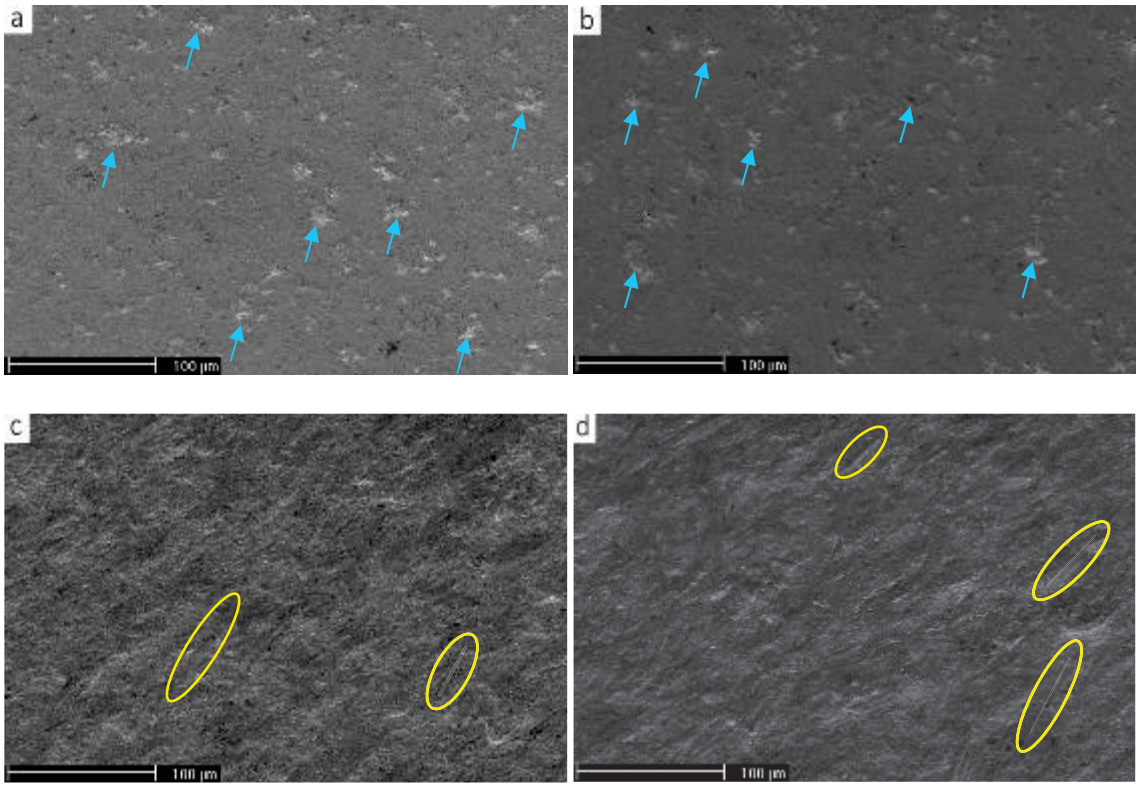

Figure 64. *SEM images of the wear surface topography of HVAF sprayed coatings a) W1M3 tested with 0.1-0.6 mm quartz size, b) W2M3 tested with 0.1-0.6 mm quartz size, c) W1M3 tested with 2-3 mm quartz size and d) W2M3 tested with 2-3 mm quartz size.*

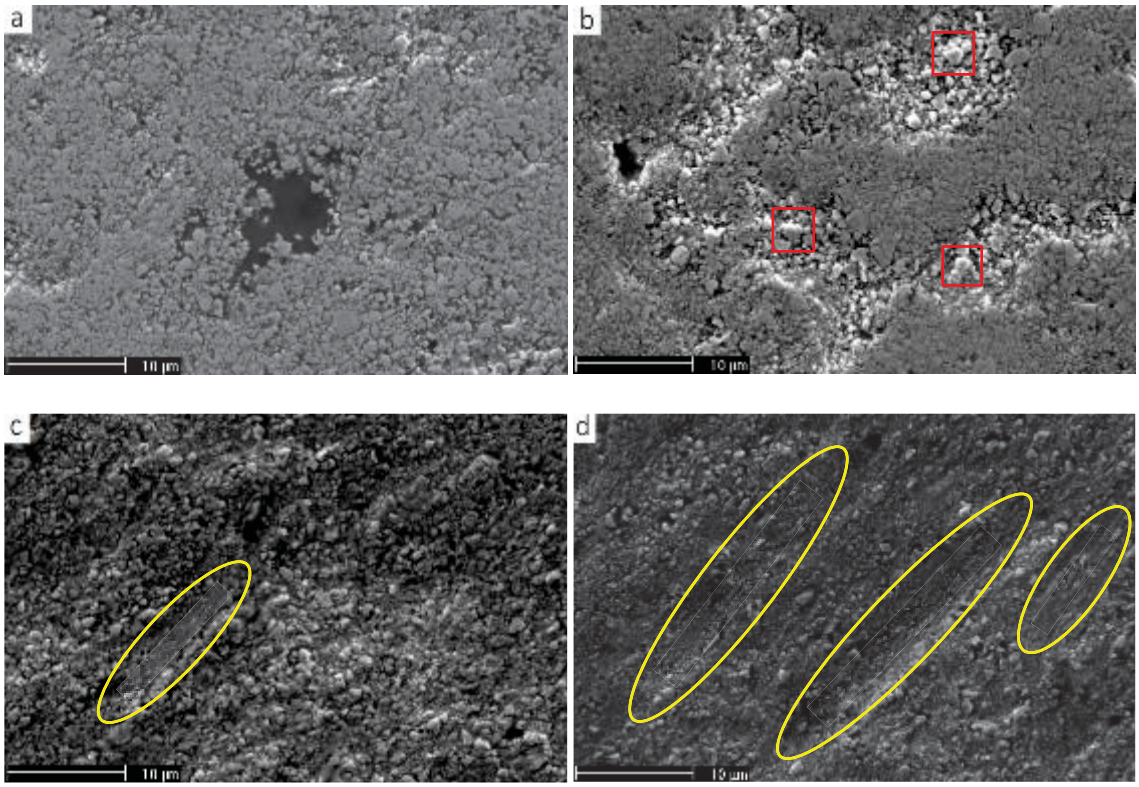

Figure 65. *Detailed SEM images of the wear surface topography of HVAF sprayed coatings a) W1M3 tested with 0.1-0.6 mm quartz size, b) W2M3 tested with 0.1-0.6 mm quartz size, c) W1M3 tested with 2-3 mm quartz size and d) W2M3 tested with 2-3 mm quartz size.*

5. DISCUSSION

In section 4 (results and analysis), coatings sprayed with the same spray process were compared. In this section the results are discussed and comparison between coatings sprayed with different techniques is presented. The analysis allows to determine the effect of the spray technology on the microstructure and performance of coatings against cavitation and slurry erosion.

5.1 Microstructure of the polished coating surface

First Cr_3C_2-25NiCr coatings are analysed and then the WC-10Co4Cr coatings. Starting with the comparison of gas and liquid HVOF processes, there was more carbon dissolution in the coatings produced with the first one. When only comparing C1DJ and C2JP, one would find more carbon diluted in the coatings sprayed with liquid fuel HVOF. This could be explained by the smaller particle size distribution used for the C2JP and its powder manufacturing process that included plasma densification. When comparing equal conditions such as C1DJ vs C1JP (same particle size and powder manufacturing process) the gas fuel HVOF spray process would produce higher levels of carbide dissolution.

Addressing the carbide size, coatings with the same particle size are compared. In the case of C1JP and C1DJ there is a higher concentration of carbides in the first one, having both of them the same powder manufacturing process. Between C2DJ and C1JP, which differ in the powder manufacturing process, the liquid fuel HVOF sprayed coating has a more uniform carbide size distribution and generally bigger carbides.

Now, if liquid fuel HVOF and HVAF sprayed coatings are compared, it is found that the latter ones have less carbon dissolution. In both processes dissolution is higher when spraying plasma densified powders and their carbides size decrease, especially in C2JP that show many areas with reduced amounts of carbides.

Finally, in gas fuelled HVOF and HVAF sprayed coatings, carbon dissolution was higher in all cases in the HVOF sprayed coatings. This agrees with the theory since HVOF works with higher temperatures, causing more carbon dissolution. The only HVAF coating that had a similar carbon dissolution was C2M3 [2].

In WC-10Co4Cr coatings, carbides size was similar no matter the spray process used. Both gas HVOF coatings had more carbon dissolution than W1JP and similar levels than W2JP, whose particle size distribution was smaller. HVAF coatings, as it was supposed, presented the lowest dissolution. It must be remembered that all comparisons done of carbon dissolution, for both coating compositions, are based on microstructural observations.

5.2 Cavitation erosion wear

Starting with Cr_3C_2-25NiCr, roughness and cavitation pitting are highest for the gas fuel HVOF sprayed coatings followed by the liquid fuel HVOF sprayed coatings. The exception was the HVAF coating C2M3 that presented similar cavity density and roughness as C1DJ, though the spacing between the peaks on C1DJ surface were found bigger. These similarities were found as well for the liquid fuel HVOF coatings, whose cavitation pitting was even slightly smaller than C2M3. Another feature found were the flat areas and fracture surfaces that denote brittle fracture, which were bigger for the gas fuel HVOF coatings and smaller with the HVAF process. Analysing the mean erosion rates, it is clear the superior cavitation resistance of liquid fuel HVOF and HVAF coatings against gas fuel HVOF coatings, while the HVAF process proved to produce coatings with the lowest volume losses.

The same trend found for Cr_3C_2-25NiCr coatings is observed also in WC-10Co4Cr coatings: gas fuel HVOF coatings present the highest roughness and porosity together with the lowest cavitation erosion resistance and HVAF samples are the best performing ones. Talking about the surface topography, gas fuel HVOF sprayed coatings are formed by blocky structures that reveal brittle fracture during cavitation erosion while liquid fuel HVOF and HVAF sprayed coatings show surfaces eroded by ductile fracture. Another feature observed is the presence of polished regions that have not been eroded yet, which occupy around 25% of the images of HVAF samples and in the case of HVOF coatings they can be found occasionally.

Therefore, it has been proven for both hardmetals that the highest cavitation erosion resistances are achieved with the HVAF process, followed by the liquid fuel HVOF technique.

5.3 Slurry erosion wear

For both hardmetals, the gas fuel HVOF process usually presented the lowest slurry erosion resistance and the HVAF process produced the best performing coatings. However, for both materials there were some exceptions that did not follow this trend. In the case of Cr_3C_2-25NiCr coatings, C1M3 presented more volume loss than C1JP in the 0.1-0.6 mm quartz size test and even higher values than C1DJ in the 2-3 mm quartz size test. The reduced slurry erosion resistance of C1M3 is related to its limited carbide dissolution that left large areas of soft metallic matrix. Regarding WC-10Co4Cr coatings, W1M3 had a slightly higher volume loss than W1JP in the 0.1-0.6 mm quartz size test, though in the SEM characterisation the liquid fuel HVOF coating seemed more eroded. Besides, in the 2-3 mm quartz size test, the liquid fuel HVOF technique appeared as the worst performing one, instead of the gas fuel HVOF technology.

6. CONCLUSIONS

Two hardmetal compositions, Cr_3C_2-25NiCr and WC-10Co4Cr, were thermally sprayed with three different thermal spray technologies: gas fuel HVOF, liquid fuel HVOF and HVAF. For each hardmetal there were six different coatings whose feedstock powder varied in particle size distribution and manufacturing process. Cavitation and slurry erosion tests were performed for these twelve samples. Volume losses were determined for the tested coatings and the eroded surfaces were characterised with SEM.

Comparing the results, some conclusion can be drawn. First of all, carbide dissolution in as-sprayed coatings was higher for those processes with a higher operating temperature, i.e. it was highest in gas fuel HVOF coatings and lowest in HVAF coatings. Regarding cavitation erosion, the HVAF spray process produced the best performing coatings with the lowest mean erosion rates, porosity and crater concentration on its eroded surfaces. Gas fuel HVOF coatings had the highest volume losses and liquid fuel HVOF sprayed coatings presented intermediate performance between the two other processes. On the other hand, the slurry erosion resistance followed the same trend observed in the cavitation tests but with some exceptions, e.g. one of the HVAF coatings of Cr_3C_2-25NiCr (C1M3) presented bigger volume loss than the HVOF coatings. In addition, the liquid fuel HVOF sprayed coatings of WC-10Co4Cr were the worst performing in the test with coarse erodent particles.

In conclusion, the shown test results indicate that the HVAF process may serve as a superior alternative to HVOF techniques in terms of cavitation and slurry erosion resistance, besides of being a more economical technology since it works with air instead of pure oxygen.

Finally, in order to continue with the research some future lines are presented:

- Additional set of slurry erosion tests should be carried out with the fine quartz size to confirm the observed results.
- SEM/BSE cross-sectional images of the coatings before and after being eroded. These micrographs would provide information about thickness, internal pores and cracks and delamination.
- Surface roughness, porosity and phase analysis of coatings. The numerical values would support the features already described in the surface micrographs.
- Analysis of the debris generated in the cavitation tests. By identifying the size and nature (carbide or metal matrix) of the particles removed, additional information is obtained to support the description of the cavitation mechanism.

REFERENCES

[1] L. Jacobs, M. M. Hyland, M. De Bonte, Study of the Influence of Microstructural Properties on the Sliding-Wear Behavior of HVOF and HVAF Sprayed WC-Cermet Coatings, Journal of Thermal Spray Technology, Vol. 8, Iss. 1, 1999, pp. 125-132.

[2] L. Jacobs, M. M. Hyland, M. De Bonte, Comparative Study of WC-Cermet Coatings Sprayed via the HVOF and the HVAF Process, Journal of Thermal Spray Technology, Vol. 7, Iss. 2, 1998, pp. 213-218.

[3] Q. Wang et al, Wear and Corrosion Performance of WC-10Co4Cr Coatings Deposited by Different HVOF and HVAF Spraying Processes, Surface & Coatings Technology, Vol. 218, Iss. 15, 2013, pp. 127-136.

[4] K. J. A. Brookes, Hardmetals and Other Hard Materials, International Carbide Data, East Barnet, Herts, UK, 1992, 198 p.

[5] H. M. Ortner, P. Ettmayer, H. Kolaska, The History of the Technological Progress of Hardmetals, International Journal of Refractory Metals and Hard Materials, Vol. 44, 2014, pp. 148-159.

[6] K. Schröter, Sintered Hardmetal Alloy and Procedure for its Fabrication, DRP 420.689, 1923.

[7] L. Berger, Coatings by Thermal Spray, in V. K. Sarin, D. Mari, L. Llanes, Comprehensive Hard Materials, Elsevier, 2004, pp. 471-506.

[8] P. Kulu, T. Pihl, Selection Criteria for Wear Resistant Powder Coatings Under Extreme Erosive Wear Conditions, Journal of Thermal Spray Technology, Vol. 11, Iss. 4, 2002, pp. 517-522.

[9] A. V. Levy, The Erosion–corrosion Behavior of Protective Coatings, Surface and Coatings Technology, Vol. 36, Iss. 1-2, 1988, pp. 387-406.

[10] P. N. Walsh, W. Tabakoff, Comparative erosion resistance of coatings intended for steam turbine components, Advances in Steam Turbine Technology for Power Generation, Vol. 10, 1990.

[11] T. Lewis, L. Sokol, E. Hanna, Optimization of Gator-gard Applied Chrome Carbide-MCrAlY Composite Overlays for Maximum Solid Particle Erosion Resistance, in Proceedings of the National Thermal Spray Conference, Orlando, Florida, USA, September 14-17, 1988. ASM International, pp. 149-154.

[12] J. P. Tu, Z. Y. Mao, J. Li, L. Z. Wang, Erosion Behavior of a Thermally Sprayed Ni–WC Coating at High Temperature, in Proceedings of the Fourth National Thermal Spray Conference, Pittsburgh, Pennsylvania, USA, 1991. ASM International.

[13] B. Q. Wang, G. Q. Geng, A. V. Levy, Erosion–corrosion of Thermal Spray Coatings, Surface and Coatings Technology, Vol. 43, 1990, pp. 859-874.

[14] P. Vuoristo, Thermal Spray Coating Processes, in S. Hashmi, Comprehensive Materials Processing, Elsevier, 2014, pp. 229-276.

[15] L. Pawlowski, Thermal Spraying Techniques, in Science and Engineering of Thermal Spray Coatings, John Wiley & Sons, West Sussex, UK, 2008, pp. 67-113.

[16] A. Vackel, G. Dwivedi, S. Sampath, Structurally Integrated, Damage-Tolerant, Thermal Spray Coatings, Journal of the Minerals, Metals & Materials Society, Vol. 67, Iss. 7, 2015, pp. 1540-1553.

[17] D. E. Crawmer, Thermal Spray Processes, in J. R. Davis, Handbook of Thermal Spray Technology, ASM International, USA, 2004, pp. 54-76.

[18] G. M. Giannini , A. C. Ducati, Plasma Stream Apparatus and Methods, US 2922869, 7.7.1958 (26.1.1960), 26 p.

[19] R. M. Gage, O. H. Nestor, D. M. Yenni, Collimated Electric Arc-powder Deposition Process, US 3016447, 2.11.1959 (9.1.1962), 7 p.

[20] A. P. Alkhimov, V. F. Korasev, A. N. Papyrin, A Method of "Cold" Gas-dynamic Deposition, Soviet Physics Doklady, Vol. 35, 1990.

[21] D. E. Crawmer, Coating Structures, Properties and Materials, in J. R. Davis, Handbook of Thermal Spray Technology, ASM International, USA, 2004, pp. 47-53.

[22] L. Baron, S. Rubio Peregrina, Characterization of Thermal Spray Coatings, Tampere University of Tecnology, Tampere, 2016, unpublished report, 13 p.

[23] Y. Itoh, M. Saitoh, M. Tamura, Characteristics of MCrAlY Coatings Sprayed by High Velocity Oxygen-Fuel Spraying System, Journal of Engineering for Gas Turbines and Power, Vol. 122, Iss. 1, 2000, pp. 43-49.

[24] H. M. Hawthorne, B. Arsenault, J. P. Immarigeon, J. G. Legoux, V. R. Parameswaran, Comparison of Slurry and Dry Erosion Behaviour of Some HVOF Thermal Sprayed Coatings, Wear, Vol. 225, 1999, pp. 825-834.

[25] B. S. Mann, V. Arya, Abrasive and Erosive Wear Characteristics of Plasma Nitriding and HVOF Coatings: Their Application in Hydro Turbines, Wear, Vol. 249, Iss. 5, 2001, pp. 354-360.

[26] G. Hou, X. Zhao, H. Zhou, J. Lu, Y. An, J. Chen, J. Yang, Cavitation Erosion of Several Oxy-fuel Sprayed Coatings Tested in Deonized Water and Artificial Seawater, Wear, Vol. 311, Iss. 1, 2014 pp. 81-92.

[27] K. J. Stein, B. S. Schorr, A. R. Marder, Erosion of Thermal Spray MCr–Cr_3C_2 Cermet Coatings, Wear, Vol. 224, Iss. 1, 1999, pp. 153-159.

[28] J. A. Picas, A. Forn, G. G. Matthäus, HVOF Coatings as an Alternative to Hard Chrome for Pistons and Valves, Wear, Vol. 261, Iss. 5, 2006, pp. 477-484.

[29] W. Rusch, Comparison of Operating Characteristics for Gas and Liquid Fuel HVOF Torches, in Proceedings of the International Thermal Spray Conference 2007, Beijing, China, May 14-16, 2007. ASM International.

[30] H. Kreye, F. Gärtner, A. Kirsten, R. Schwetzke, High-velocity oxy-fuel flame spraying state of the art, prospects and alternatives, in 5th Colloquium on High Velocity Flame Spraying, GTS e.V., Erding, Germany, November 16-17, 2000.

[31] J. A. Browning, Maximum Combustion Energy Conversion Air Fuel Internal Burner, US 5120582, 16.1.1991 (9.6.1992), 6 p.

[32] J. A. Browning, Hypervelocity Impact Fusion - A Technical Note, Journal of Thermal Spray Technology, Vol. 1, Iss. 4, 1992 pp. 289-292.

[33] L. Berger, R. Puschmann, J. Spatzier, S. Matthews, Potential of HVAF Spray Processes, Thermal Spray Bulletin, Vol. 65, Iss. 1, 2013, pp. 16-20.

[34] J. A. Browning, Thermal Spray Method Utilizing In-transit Powder Particle Temperatures Below Their Melting Point, US 5271965, 15.1.1992 (6.81993), 8 p.

[35] A. Verstak, G. Kusinki, High Velocity Air-fuel Spraying and Its Applications in Oil and Gas Industry, in Proceedings of International Thermal Spray Conference 2012, Houston, Texas, USA, May 21-24, 2012. ASM International.

[36] Standard Test Method for Cavitation Erosion Using Vibratory Apparatus, ASTM International, ASTM G32-16, USA, 2016, 20 p.

[37] G. Stachowiak, A. Batchelor, Abrasive, Erosive and Cavitation Wear, in Engineering Tribology, Elsevier, 2011, pp. 525-607.

[38] Y. Wu, S. Hong, J. Zhang, Z. He, W. Guo, Q. Wang, G. Li, Microstructure and Cavitation Erosion Behavior of WC–Co–Cr Coating on 1Cr18Ni9Ti Stainless Steel by HVOF Thermal Spraying, International Journal of Refractory Metals and Hard Materials, Vol. 32, 2012, pp. 21-26.

[39] W. Yuping, L. Pinghua, C. Chenglin, W. Zehua, C. Ming, H. Junhua, Cavitation Erosion Characteristics of a Fe–Cr–Si–B–Mn Coating Fabricated by High Velocity Oxy-fuel (HVOF) Thermal Spray, Materials Letters, Vol. 61, Iss. 8, 2007, pp. 1867-1872.

[40] J. He, F. G. Hammitt, Velocity Exponent and Cavitation Number for Venturi Cavitation Erosion of 1100-O Aluminum and 1018 Carbon Steel, Wear, Vol. 80, Iss. 1, 1982, pp. 43-58.

[41] B. S. Mann, Boronizing of Cast Martensitic Chromium Nickel Stainless Steel and Its Abrasion and Cavitation-erosion Behaviour, Wear, Vol. 208, Iss. 1, 1997, pp. 125-131.

[42] B. S. Mann, V. Arya, An Experimental Study to Corelate Water Jet Impingement Erosion Resistance and Properties of Metallic Materials and Coatings, Wear, vol. 253, Iss. 5, 2002, pp. 650-661.

[43] H. S. Grewal, H. Singh, Slurry Erosion Behaviour of Thermal Spray Coatings, in M. Roy, J. P. Davim, Thermal Sprayed Coatings and their Tribological Peroformances, IGI Global, Hershey, Pennsylvania, 2015, pp. 268-293.

[44] I. M. Hutchings, R. E. Winter, Particle Erosion of Ductile Metals: A Mechanism of Material Removal, Wear, Vol. 27, Iss. 1, 1974, pp. 121-128.

[45] D. K. Goyal, H. Singh, H. Kumar, V. Sahni, Slurry Erosive Wear Evaluation of HVOF-Spray Cr_2O_3 Coating on Some Turbine Steels, Journal of Thermal Spray Technology, Vol. 21, Iss. 5, 2012, pp. 838-851.

[46] H. S. Grewal, H. S. Arora, A. Agrawal, H. Singh, S. Mukherjee, Slurry Erosion of Thermal Spray Coatings: Effect of Sand Concentration, Procedia Engineering, Vol. 68, 2013, pp. 484-490.

[47] D. K. Goyal, H. Singh, H. Kumar, V. Sahni, Slurry Erosion Behaviour of HVOF Sprayed WC–10Co–4Cr and Al_2O_3+13TiO_2 Coatings on a Turbine Steel, Wear, Vol. 289, 2012, pp. 46-57.

[48] Standard Terminology Relating to Wear and Erosion, ASTM International, ASTM G40-87, USA, 1987, 7 p.

[49] H. S. Grewal, A. Agrawal, H. Singh, Design and Development of High-Velocity Slurry Erosion Test Rig Using CFD, Journal of Materials Engineering and Performance, Vol. 22, Iss. 1, 2013, pp. 152-161.

[50] A. Abouel-Kasem, Y. M. Abd-Elrhman, K. M. Emara, S. M. Ahmed, Design and Performance of Slurry Erosion Tester, Journal of Tribology, Vol. 132, Iss. 2, 2010.

[51] N. Ojala, K. Valtonen, P. Kivikytö-Reponen, P. Vuorinen, V. T. Kuokkala, High Speed Slurry-pot Erosion Wear Testing with Large Abrasive Particles, Finnish Journal of Tribology, Vol. 33, Iss. 1, 2015, pp. 36-44.

[52] L. Thakur, N. Arora, R. Jayaganthan, R. Sood, An Investigation on Erosion Behaviour of HVOF Sprayed WC-CoCr Coatings, Vol. 258, Iss. 3, 2011, pp. 1225-1234.

[53] J. B. Zu, I. M. Hutchings, G. T. Burstein, Design of a Slurry Erosion Test Rig, Wear, Vol. 140, Iss. 2, 1990, pp. 331-344.

[54] Q. Fang, H. Xu, P. S. Sidky, M. G. Hocking, Erosion of Ceramic Materials by a Sand/Water Slurry Jet, Wear, Vol. 224, Iss. 2, 1999, pp. 183-193.

[55] Y. Li, G. T. Burstein, I. M. Hutchings, The Influence of Corrosion on the Influence of Aluminum by Aqueous Silica Slurries, Wear, Vol. 186, 1995, pp. 515-522.

[56] F. I. Lin, H. S. Shao, Effect of Impact Velocity on Slurry Erosion and a New Design of Slurry Erosion Tester, Wear, Vol. 143, Iss. 2, 1991, pp. 231-240.

[57] Q. Wang, Z. Tang, L. Cha, Cavitation and Sand Slurry Erosion Resistances of WC-10Co-4Cr Coatings, Journal of Materials Engineering and Performance, Vol. 24, Iss. 6, 2015, pp. 2435-2443.

[58] J. Postlethwaite, S. Nesic, Erosion in Disturbed Liquid/Particle Pipe Flow: Effect of Flow Geometry and Particle Surface Roughness, Corrosion, Vol. 49, Iss. 10, 1993, pp. 850-857.

[59] M. M. Salama, An Alternative to API 14E Erosional Velocity Limits for Sand Laden Fluids, Journal of Energy Resources Technology, Vol. 122, Iss. 2, 2000, pp. 71-77.

[60] A. Elkholy, Prediction of Abrasion Wear for Slurry Pump Materials, Wear, Vol. 84, Iss. 1, 1983, pp. 39-49.

[61] A. V. Levy, G. Hickey, Liquid-Solid Particles Slurry Erosion of Steels, Wear, Vol. 117, Iss. 2, 1987, pp. 129-146.

[62] C. C. Berndt, Material Production Processes, in J. R. Davis, Handbook of Thermal Spray Technology, ASM International, USA, 2004, pp. 147-158.

[63] D. R. Lide, Section 4: Properties of the Elements and Inorganic Compounds, in CRC Handbook of Chemistry and Physics, CRC Press, Boca Raton, Florida, USA, 2003.

[64] G. Lawes, Scanning Electron Microscopy and X-Ray Microanalysis, John Wiley & Sons, New York, USA, 1987.

[65] V. Matikainen, Effect of Nozzle Geometry on the Microstructure and Properties of HVAF Sprayed Hard Metal Coatings, International Thermal Spray Conference 2017 (Presentation), Düsseldorf, Germany, June 7-9, 2017.

[66] V. Matikainen, H. Koivuluoto, P. Vuoristo, Effect of Nozzle Geometry on the Microstructure and Properties of HVAF Sprayed Hard Metal Coatings, in Proceedings of International Thermal Spray Conference 2017, Düsseldorf, Germany, June 7-9, 2017. ASM International, pp. 333-338.